Charles University
Faculty of Science

Modeling of Chemical Properties of Nano- and Biostructures

Ing. Marek Pederzoli, M.Sc.

Ab initio molecular dynamics with non-adiabatic and spin-orbit effects applied to time-dependent fluorescence

Ab initio molekulová dynamika s neadiabatickými a spin-orbitálními efekty aplikovaná na časově závislou fluorescenci

DOCTORAL THESIS

Supervisor: Doc. Mgr. Jiří Pittner Dr. rer. nat., DSc.

Prague, 2018

Prohlášení

Prohlašuji, že jsem nepředložil práci ani její podstatnou část k získání jiného nebo stejného akademického titulu. Práci jsem zpracoval samostatně a uvedl všechny použité informační zdroje a literaturu.

_____

CONTENTS

Contents **Page No.**

Dedication

To my girlfriend Jana, for her love, patience and support.

I would also like to thank all my friends, colleagues and coworkers for help and collaboration, especially my supervisor, Dr. Jiří Pittner, for leading this project. Last, but not least, my sincere gratitude also goes to my family, particularly my mother who always encouraged me in my pursuit of science and supported me during the entire duration of my studies.

Abstract

Fluorescent probes are essential for many experimental techniques in biochemistry and microbiology. Accurate simulations of these molecules are theoretically challenging as they can involve conical intersections and intersystem crossings as well as interactions with the environment.

This thesis is a compilation of papers dealing with development, implementation, and application of ab initio molecular dynamics techniques with non-adiabatic and spin-orbit interactions that can be used to model fluorescent probes not only in the gas phase but also in the complex molecular environment of biomembranes.

Initial work involves a study of 9H-adenine using ab initio MD with non-adiabatic effect using time-dependent density functional theory and two single reference methods CC2 and ADC(2). The central part of the thesis discusses the implementation of spin-orbit coupling into surface hopping dynamics with application to deactivation of thiophene and selenophene. Further applications include studying spectra and dynamics of the fluorescence probe Prodan in the gas phase and in solution, and simulation of absorption spectra of Laurdan in biomembranes. Other systems are being investigated and will be published soon. My implementation has become a part of the official Newton-X program package.

Foreword

This thesis is a compilation of research papers related to the project Ab initio molecular dynamics with non-adiabatic and spin-orbit effects applied to time-dependent fluorescence in the study program Modeling of Chemical Properties of Nano- and Biostructures.

In this project, I have touched several areas of research and I believe the results may be interesting and useful for researchers involved in molecular simulations of ultrafast processes, photochemists and experimentalists using fluorescence probes and fluorescence spectroscopy.

The thesis is structured as follows: Chapter 1 serves as a general introduction to molecular modeling and simulations. In Chapter 2, I will introduce the basic concept of ab initio molecular dynamics, concentrating on trajectory-based approaches, mainly surface hopping. Chapter 3 describes incorporating spin-orbit coupling into surface hopping dynamics. Chapter 4 provides some basic background in photochemistry needed for our applications, especially about fluorescence and fluorescent probes. Chapter 5 covers the main results of the individual papers and Chapter 6 provides a final summary and future applications.

Chapter 1

Molecular modeling and computer simulations of molecules

Molecular modeling is a general process with the aim to understand molecules and their behavior using models, i.e. simplified representations of the system. These representations may have many forms including physical (e.g., ball bearings used to represent molecules of a liquid), purely mathematical and computational in which the underlying mathematical model is implemented into computer programs. Using these models, we may carry out simulations in which we study the behavior and properties of the system, often in relation to selected initial conditions and parameters of the model.

The field of molecular modeling is evolving very rapidly. The advent of modern computers revolutionized the field, and their ever-increasing power enables us not only to study larger systems and more complex processes but also to use much more advanced methods. We now live in an exciting era for computational chemistry; the new technologies allow us to transition from simple models of limited validity to a fully quantum mechanical description of electronic interactions. The computer simulations on such level may provide a very useful complement (or even a substitute) for real experiments and are becoming increasingly popular. One of the most prominent methods of molecular modeling is molecular dynamics (MD), which may be defined

as a computer simulation of the evolution of molecules and atoms in time. MD simulations may be carried out at various levels of theory ranging from classical physics to fully quantum-mechanical description. If the reader is unfamiliar with molecular modeling and MD, he or she may refer to a classic book of Allen and Tildesley[1] or a more recent one by Frenkel and Smit.[2]

This dissertation thesis is a compilation of papers dealing with development and applications of state-of-art methods of ab initio molecular dynamics including non-adiabatic and spin-orbit (SO) coupling. These approaches will be introduced in some detail in the following chapters.

Chapter 2

Ab initio MD with non-adiabatic and SO effects: An introduction

In this chapter, I will introduce the main theoretical concepts and methods used in ab initio MD with non-adiabatic and SO effects. First, ab initio MD within the Born-Oppenheimer (B-O) approximation will be discussed. To go beyond the B-O approximation, several routes can be taken; here we will only concentrate on the trajectory-based approach used in our group, namely Tully's surface hopping. In the next section, SO coupling will be introduced to surface hopping dynamics. Finally, at the end of the chapter, I will introduce the quantum mechanics/molecular mechanics approach (QM/MM) used to include explicit solvent into the simulations.

2.1 Ab initio MD

In non-relativistic quantum chemistry we aim at solving the Schrödinger equation (SE):

$$\hat{H}\Psi = E\Psi, \tag{2.1}$$

where Ψ is the wave function, $\hat{H}$ is the Hamiltonian, an operator of the total energy, and E is the total energy of the system. The most commonly used form of the Hamiltonian, also known as molecular Coulomb Hamilto-

nian, usually takes the following form (in atomic units):

$$\hat{H} = -\frac{1}{2}\sum_i \nabla_i^2 - \frac{1}{2M_A}\sum_A \nabla_A^2 - \sum_{A,i}\frac{Z_A}{r_{Ai}} + \sum_{A>B}\frac{Z_A Z_B}{R_{AB}} + \sum_{i>j}\frac{1}{r_{ij}}. \quad (2.2)$$

The terms are in this order: the kinetic energy of the electrons, the kinetic energy of the nuclei, Coulombic interactions of electrons with nuclei, Coulombic interactions of nuclei, and Coulombic interactions of electrons. More compactly:

$$\hat{H} = \hat{T}_{\mathrm{N}}(\mathbf{R}) + \hat{T}_{\mathrm{e}}(\mathbf{r}) + \hat{V}_{\mathrm{eN}}(\mathbf{r},\mathbf{R}) + \hat{V}_{\mathrm{NN}}(\mathbf{R}) + \hat{V}_{\mathrm{ee}}(\mathbf{r}), \quad (2.3)$$

where $\mathbf{R}$ is the set of nuclear coordinates and $\mathbf{r}$ is the set of electronic coordinates.

2.1.1 The Born-Oppenheimer approximation

The Born-Oppenheimer (B-O) approximation plays a central role in quantum chemistry. It allows us to separate the electronic and nuclear degrees of freedom, which is necessary for solving the SE for all but the smallest of molecules. The justification of the separation can be summarized like this: For the fast-moving electrons, the much heavier nuclei seem static. The nuclei, on the other hand, move in the averaged field created by the fast-moving electrons.

If we solve the electronic SE for some fixed nuclear coordinates $\mathbf{R}$:

$$\hat{H}_{\mathrm{el}}\phi_{\mathrm{el}}(\mathbf{r};\mathbf{R}) = E_{\mathrm{el}}\phi_{\mathrm{el}}(\mathbf{r};\mathbf{R}), \quad (2.4)$$

where E_{el} is the electronic energy, $\phi_{\mathrm{el}}(\mathbf{r};\mathbf{R})$ is the electronic wave function, which depends only parametrically on $\mathbf{R}$ and the electronic Hamiltonian is usually taken in the form:

$$\hat{H}_{\mathrm{el}} = \hat{T}_{\mathrm{e}}(\mathbf{r}) + \hat{V}_{\mathrm{eN}}(\mathbf{r},\mathbf{R}) + \hat{V}_{\mathrm{NN}}(\mathbf{R}) + \hat{V}_{\mathrm{ee}}(\mathbf{r}), \quad (2.5)$$

expanding the solution of the full SE into the basis of the eigenstates of the

electronic SE equation, the SE for the nuclei can be shown to become

$$\left[\hat{T}_{\mathrm{N}} + E_{\mathrm{el}}\right] \chi_k + \sum_l \left(\langle \psi_l | \hat{T}_{\mathrm{N}} | \psi_k \rangle - \sum_A \frac{1}{M_A} \langle \psi_l | \nabla_A | \psi_k \rangle \cdot \nabla_A \right) \chi_k = E_k \chi_k, \tag{2.6}$$

where χ_k is the nuclear wave function and the terms in the parentesis are the non-adiabatic coupling terms. After neglecting the coupling terms we obtain:

$$\left[\hat{T}_{\mathrm{N}} + E_{\mathrm{el}}\right] \chi_k = E_k \chi_k, \tag{2.7}$$

which is the essence of the B-O approximation.

2.1.2 The Born-Oppenheimer MD

Solving the full time dependent SE:

$$\mathrm{i}\frac{\partial}{\partial t}\Psi = \hat{H}\Psi, \tag{2.8}$$

for both the electrons and the nuclei is possible only for very small systems with a few degrees of freedom. For larger systems, some approximations have to be made. We can start with the B-O approximation to separate nuclear and electronic motion and treat the nuclei classically while solving the electronic SE 2.4 using various methods of quantum chemistry. The Newton equations of motion then become:

$$m_i \frac{d^2 R_i}{dt^2} = f_i = -\nabla_{R_i} \left\langle \Psi_{\mathrm{el}} \middle| \hat{H}_{\mathrm{el}} \middle| \Psi_{\mathrm{el}} \right\rangle, \tag{2.9}$$

2.2 Including non-adiabatic effects

There are several approximate methods to include the non-adiabatic effects into classical molecular dynamics; the most common ones are variations of Ehrenfest method[3] and various version of surface hopping.[4] In this work, we will be using Tully's surface hopping[5, 6] method briefly described below.

The main idea of Tully's method is that the nuclei always move classi-

cally on a single potential energy surface (as in the B-O approximation), but they are allowed to switch the surface when necessary (this is referred to as performing a 'hop' or 'hopping'). After expanding the electronic wave function in the basis of geometry-dependent adiabatic states with time-dependent coefficients:

$$\phi(t) = \sum_j c_j(t)\phi_j(\mathbf{R}(t)), \tag{2.10}$$

the following equation for the coefficients can be obtained:

$$\mathrm{i}\dot{c}_k(t) = \sum_j \left[E_j\delta_{kj} - \mathrm{i}\mathbf{v}(t)\cdot\langle\phi_k\left|\nabla_{\mathbf{R}}\right|\phi_j\rangle\right] c_j(t). \tag{2.11}$$

The hopping probability is proportional to the variation of the quantum populations, usually with the additional constraint that the number of hopping events is minimized, therefore the method is called the fewest switches algorithm.[5] The hopping probabilities between states k and j can be calculated as follows:

$$p(k\to j) = \frac{b_{jk}\Delta t}{c_k c_k^*}, \tag{2.12}$$

where

$$b_{jk} = 2\Im(c_k^* c_l E_k\delta_{kl}) - 2\Re(c_k^* c_l \mathbf{v}\cdot\langle\phi_k\left|\nabla_{\mathbf{R}}\right|\phi_j\rangle), \tag{2.13}$$

where $\langle\phi_k\left|\nabla_{\mathbf{R}}\right|\phi_j\rangle$ is the non-adiabatic coupling vector for the adiabatic states k and j. The scalar product of $\langle\phi_k\left|\nabla_{\mathbf{R}}\right|\phi_j\rangle$ with velocities expresses the non-adiabatic coupling between the adiabatic surfaces j and k; the product is also known as the time derivative coupling. Using the chain rule, we can obtain

$$\mathbf{v}\cdot\langle\phi_k\left|\nabla_{\mathbf{R}}\right|\phi_j\rangle = \langle\phi_k|\frac{\partial}{\partial t}|\phi_j\rangle. \tag{2.14}$$

A stochastic hopping procedure is employed: a uniform random number r from the interval $0 \le r \le 1$ is selected and the hop to state j is performed if

$$\sum_{i=1}^{j-1} p(k\to i) < r \le \sum_{i=1}^{j} p(k\to i) \tag{2.15}$$

The algorithm for surface hopping dynamics can be summarized like this:

1. For a nuclear geometry at a given time step, the electronic SE is solved; energies, gradients and non-adiabatic coupling vectors are calculated.
2. The gradient of the current potential energy surface is used to update the nuclear geometry according to the Newton equations.
3. The coefficients $c_j(t)$ are propagated using the time-dependent SE.
4. Hopping probabilities $p(k \to j)$ are computed.
5. If a hop is performed, the velocities are adjusted to conserve energy.
6. The steps 1.-5. are repeated until the end of the trajectory.
7. The whole ensemble of trajectories is computed to obtain the "classical wave packet."

2.3 Including spin-orbit coupling

In principle, to fully include spin-orbit effects, one should employ the relativistic Dirac-Coulomb Hamiltonian; this would, however, be extremely computationally expensive and only possible for very small systems. For small to moderate values of spin-orbit coupling, the following approximation may be used as a starting point: the total molecular Hamiltonian is assumed to be in the form

$$\hat{H}^{\mathrm{tot}} = \hat{H}^{\mathrm{MCH}} + \hat{H}^{\mathrm{SO}}, \tag{2.16}$$

a sum of the molecular Coulomb Hamiltonian, $\hat{H}^{\mathrm{MCH}}$, depending on the electronic structure method used, and the spin-orbit Hamiltonian $\hat{H}^{\mathrm{SO}}$.

The electronic wave function may be propagated either in the basis of adiabatic states, i.e., the eigenstates of $\hat{H}^{\mathrm{MCH}}$ or in the spin-mixed eigenstates of the total molecular Hamiltonian $\hat{H}^{\mathrm{tot}}$; the first approach is usually appropriate only for small values of spin-orbit coupling, while the latter may be used even for moderate coupling strengths. I will discuss both of these approaches briefly.

2.3.1 Propagation of the electronic wave function in the basis of adiabatic states

The MD trajectories can be propagated on surfaces corresponding to N_s calculated eigenstates of $\hat{H}^{\mathrm{MCH}}$, which form a truncated basis for the multi-configurational electronic wave function Ansatz:

$$\Phi(\mathbf{r}, \mathbf{R}, t) = \sum_{i=1}^{N_s} c_i(t)\phi_i(\mathbf{r}; \mathbf{R(t)}, t). \tag{2.17}$$

Inserting Eq (2.17) into the time-dependent Schrödinger equation we can obtain:

$$\frac{dc_k(t)}{dt} = \sum_j \left[-\mathrm{i} \underbrace{(E_j^{\mathrm{MCH}}\delta_{kj} + \langle\phi_k|H^{\mathrm{SO}}|\phi_j\rangle)}_{H_{kj}^{\mathrm{tot}}(R(t))} - \dot{\boldsymbol{R}}(t) \cdot \underbrace{\langle\phi_k|\nabla_{\mathbf{R}}|\phi_j\rangle}_{K_{kj}(R(t))}, \right] c_j(t) \tag{2.18}$$

or, in matrix form,

$$\dot{\boldsymbol{c}} = -(\mathrm{i}\boldsymbol{H}^{\mathrm{tot}} + \dot{\boldsymbol{R}} \cdot \boldsymbol{K})\boldsymbol{c}, \tag{2.19}$$

where $\boldsymbol{K}$ is the non-adiabatic coupling vector.

It is important to note, that in Eqs (2.18) and (2.19), every component of a triplet state has its own coefficient $c_i(t)$, as opposed to the commonly used approach,[7–14] where the triplet components are taken to be a single state with a single coefficient - a simplification that has been shown to be incorrect in general.[15] The hopping probabilities within the fewest switches approach for hops between the multiplet components are

$$p(k \to j) = \max\left\{ \frac{2\Delta t}{c_k c_k^*} \left[\Im(c_k^* c_l H_{kj}^{\mathrm{tot}}) - \Re(c_k^* c_l \dot{\boldsymbol{R}} \cdot \boldsymbol{K}) \right], 0 \right\}. \tag{2.20}$$

The usual stochastic algorithm is used. The total population of the multiplet states at any time step are then obtained as the sum of populations of their components during postprocessing of the trajectories.

2.3.2 Propagation of the electronic wave function in the diagonal representation

It is often advantageous[15, 16] to perform the dynamics in the basis of the spin-mixed eigenvectors of the full $\boldsymbol{H}^{\mathrm{tot}}$ matrix (the reasons will be explained in Section 2.3.3). The corresponding representation of the Hamiltonian is then called "diagonal representation," as it is obtained by diagonalization of $\boldsymbol{H}^{\mathrm{tot}}$ with a unitary transformation matrix $\boldsymbol{U}$:

$$\boldsymbol{U}^{\dagger}\boldsymbol{H}^{\mathrm{tot}}\boldsymbol{U} = \bar{\boldsymbol{H}}^{\mathrm{tot}} \equiv \boldsymbol{E}^{\mathrm{tot}}. \tag{2.21}$$

The "diagonal basis" of $\hat{H}^{\mathrm{tot}}$ eigenfunctions ψ_i can be written as:

$$\langle\psi_j|\hat{H}^{\mathrm{tot}}|\psi_i\rangle = E_i^{\mathrm{tot}}\delta_{ij}; \quad |\psi_i\rangle = \sum_j U_{ji}|\phi_j\rangle \tag{2.22}$$

and the time-dependent coefficients then become

$$\bar{\boldsymbol{c}} = \boldsymbol{U}^{\dagger}\boldsymbol{c}; \quad \boldsymbol{c} = \boldsymbol{U}\bar{\boldsymbol{c}}. \tag{2.23}$$

Propagation of the $\bar{c}$ coefficients in the "diagonal basis" is then

$$\begin{aligned}
\frac{d}{dt}\bar{\boldsymbol{c}} &= \boldsymbol{U}^{\dagger}\frac{d\boldsymbol{c}}{dt} + \frac{d\boldsymbol{U}^{\dagger}}{dt}\boldsymbol{U}\bar{\boldsymbol{c}} = \boldsymbol{U}^{\dagger}\frac{d\boldsymbol{c}}{dt} - \boldsymbol{U}^{\dagger}\frac{d\boldsymbol{U}}{dt}\bar{\boldsymbol{c}} \\
&= -\boldsymbol{U}^{\dagger}(\mathrm{i}\boldsymbol{H}^{\mathrm{tot}} + \dot{\boldsymbol{R}}\cdot\boldsymbol{K})\boldsymbol{U}\bar{\boldsymbol{c}} - \boldsymbol{U}^{\dagger}\frac{d\boldsymbol{U}}{dt}\bar{\boldsymbol{c}} \\
&= -(\mathrm{i}\boldsymbol{E}^{\mathrm{tot}} + \dot{\boldsymbol{R}}\cdot\bar{\boldsymbol{K}} + \boldsymbol{U}^{\dagger}\frac{d\boldsymbol{U}}{dt})\bar{\boldsymbol{c}} \equiv \boldsymbol{A}\bar{\boldsymbol{c}},
\end{aligned} \tag{2.24}$$

where $\bar{\boldsymbol{K}} = \boldsymbol{U}^{\dagger}\boldsymbol{K}\boldsymbol{U}$ are the transformed non-adiabatic couplings and I introduced the "propagator matrix"

$$\boldsymbol{A} = -(\mathrm{i}\boldsymbol{E}^{\mathrm{tot}} + \dot{\boldsymbol{R}}\cdot\bar{\boldsymbol{K}} + \boldsymbol{U}^{\dagger}\frac{d\boldsymbol{U}}{dt}). \tag{2.25}$$

For a short time step Δt, when $\boldsymbol{A}$ can be considered constant, the coeffi-

cients can be propagated as

$$\bar{\boldsymbol{c}}(t+\Delta t) = \exp\left[\boldsymbol{A}\Delta t\right]\bar{\boldsymbol{c}}(t) \tag{2.26}$$

The propagation in the diagonal representation has been suggested in Ref,[16] however, the implementation is not straightforward. The term $d\boldsymbol{U}/dt$ can cause numerical problems due to arbitrary phases and unitary rotations among degenerate eigenvalues and other problems involving changes in the order of states in the diagonal representation. A solution to this problem was proposed four years later by Gonzalez et al.,[17] which avoids calculation of this term altogether by propagating the coefficients in the MCH representation using a "3-step propagator" approach:

1. transform $\bar{\boldsymbol{c}}(t) \rightarrow \boldsymbol{c}(t)$
2. propagate in the MCH basis, $\boldsymbol{c}(t) \rightarrow \boldsymbol{c}(t+\Delta t)$
3. transform $\boldsymbol{c}(t+\Delta t) \rightarrow \bar{\boldsymbol{c}}(t+\Delta t)$.

The corresponding propagation equation is

$$\bar{\boldsymbol{c}}(t+\Delta t) = \boldsymbol{U}^{\dagger}(t+\Delta t)\exp\left[-(\mathrm{i}\boldsymbol{H}^{\mathrm{tot}} + \dot{\boldsymbol{R}}\cdot\boldsymbol{K})\Delta t\right]\boldsymbol{U}(t)\bar{\boldsymbol{c}}(t) \tag{2.27}$$

We have developed 2 different approaches to resolve the issues with the $d\boldsymbol{U}/dt$ term, which will be discussed in Chapter 4.

2.3.3 MCH vs diagonal representation

In purely quantum-mechanical calculations, the choice of the representation should not matter, as long as the corresponding electronic bases span the same subspace, however, in the semi-classical surface hopping approach, the representations are no longer equivalent.[18]

In the majority of the previous works,[7–13, 19–21] the dynamics was done in the MCH representation, where the total transition probabilities between spin multiplets are not rotationally invariant.[18] This artifact may be eliminated by reducing each multiplet to one rotationally invariant state that

interacts through SO coupling with the other multiplets, but this reduction is complicated and only applicable to simplest cases involving few states.[15] The other possibility, used in our work, is keeping the multiplet coefficients separate and treating the components as separate states in the surface hopping procedure.

The second problem of MCH representation is that the potential energy surfaces no longer accurately represent the energetics of the molecule when the SO coupling is large and splitting of the surfaces is non-negligible.[18] The gradients are even more sensitive to this effect, which may cause discrepancies even for a moderate strength of SO coupling. For example, consider a system where most of the population is in a singlet state in the MCH representation. This population may, however, be distributed into several diagonal states of partly triplet character. The diagonal gradient of the active state would then contain contributions from the triplet states which may in general lead the trajectory to regions of the potential energy surface not adequately sampled by the MCH representation. Note that the singlet and triplet states are only approximations obtained from the non-relativistic Hamiltonian, which would not be considered at all if the fully-relativistic 4-component formalism of Dirac equation was used; hence the diagonal representation should be closer to physical reality and therefore preferable. However, the necessity to calculate all the gradients makes the dynamics in the diagonal representation much more computationally demanding than the MCH approach. To lower the computational cost, I have recently implemented a gradient selection scheme which lowers the cost significantly and which will be published soon.

2.4 The QM/MM approach

QM/MM, or more generally hybrid gradient, MD methods allow treating different parts of the system at different levels of theory, allowing efficient simulation of larger systems. There is a vast amount of literature reviewing these methods, especially we can refer to Refs.[22–25] Here, I will briefly describe the main aspects of the implementation of QM/MM used in this work (a more detailed discussion of the hybrid gradient MD as implemented in the

Newton-X[26] program system can be found in Ref[25]).

The atoms of the whole system are divided into disjoint regions. In the case of QM/MM, there are two regions: The QM region is treated with quantum chemical methods, while the MM part is described using a force field. In principle, the division into subsystems may be completely arbitrary, and part of the molecule may belong to the QM region, while the other part into the MM region. There are several possibilities how to treat incomplete molecules in this case. Newton-X employs the "hydrogen capping" approach,[27] where the missing molecular fragments are substituted by hydrogen atoms. Typically, it is better to avoid complications caused by the cross-region bonds. In our QM/MM simulations discussed in this thesis, the QM region always contained the whole studied molecule, possibly with a few nearest solvent molecules, while the rest of the solvent was assigned to the MM region. Therefore, in the following, I will assume that there are no incomplete molecular fragments in any of the regions.

The implementation in Newton-X follows the subtractive scheme, where the total energies, and consequently the gradients, are given by

$$E^{\text{System}}_{\text{QM/MM}} = E^{\text{QM region}}_{\text{QM method}} + E^{\text{System}}_{\text{MM method}} - E^{\text{QM region}}_{\text{MM method}}. \tag{2.28}$$

The third term ensures that no interaction will be double counted.[22] Optionally, if the quantum-chemical program allows this, the point charges of the MM subsystem may be included into the QM region (and excluded from the MM force field); this approach is called electrostatic embedding. When electrostatic embedding is not available, mechanical embedding is used, where the Coulomb interactions for the whole system is calculated using the classical force field and the double counting for the QM subsystem is removed by the subtractive scheme.

Chapter 3

Basic concepts of fluorescence spectroscopy

Fluorescence spectroscopy is a very broad sub-field of spectroscopy. It includes a large number of specialized techniques most of which are outside the scope of this thesis but are essential for modern research in many areas of biochemistry and microbiology. In this chapter, I will briefly introduce some of the basic underlying concepts needed for the study of fluorescent probes and to explain why SO coupling may be important to describe their dynamics accurately.

3.1 Basic terminology

Fluorescence is simply a process of emission of light by a molecule (called fluorophore), that was previously excited by absorption of radiation.

In fluorescence spectroscopy, we excite the sample containing fluorophoric molecules by light of a known frequency and we can measure the frequency and intensity of the emitted light as a function of time.

The electronic transitions relevant for fluorescence can be described using the well-known Jablonski diagram, shown in Fig 3.1. Briefly: the molecule is excited to a singlet state. From here it normally undergoes a fast internal conversion to the lowest singlet excited state before it emits the photon of a longer wavelength. Alternatively, the molecule may undergo an intersystem

crossing to a state of different multiplicity, usually an excited triplet state. From here, it usually again undergoes an internal conversion and remains in the lowest triplet state until phosphorescence occurs.

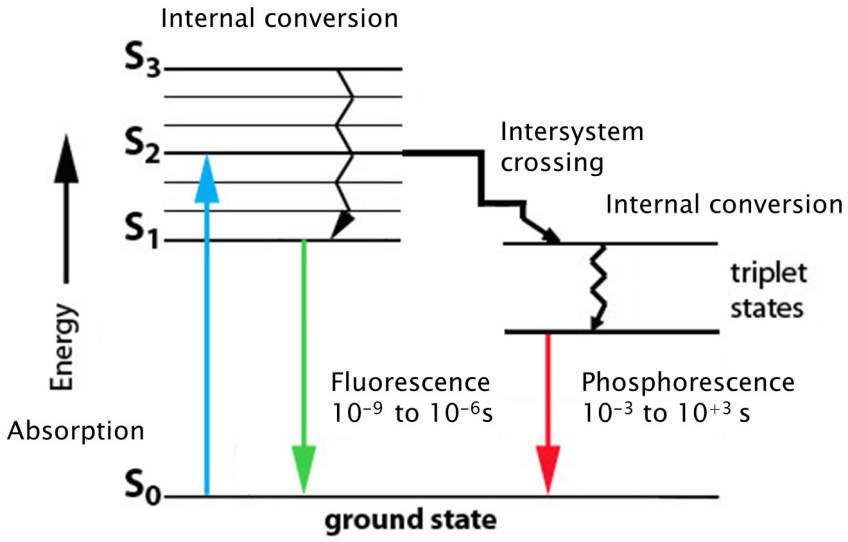

Figure 3.1: Jablonski diagram

Absorption of photons is a very rapid process during which the movement of the nuclei can usually be neglected. However, during the fluorescence lifetime, e.i., the average time that the molecule spends in the excited state before the emission of a photon, many processes may influence the emission spectrum. From the spectrum, we can then obtain information about the static and dynamic properties of the fluorophore and also about the surrounding of the molecule.

3.1.1 Fluorescence quantum yield

Quantum yield, Φ (not to be confused with the wave function), describes the efficiency of the fluorescence process and can be defined simply as the ratio of the number of photons emitted to the number of photons absorbed.

$$\Phi = \frac{N_{\text{emitted}}}{N_{\text{absorbed}}}. \tag{3.1}$$

Equivalently, it relates how the rate of spontaneous emission compares to the sum of rates of all the possible deactivation processes.

3.1.2 Quenching

Quenching refers to any deactivation process which lowers the fluorescence quantum yield. It may be caused by several processes including collisions with another molecule, resonant energy transfer, or an intersystem crossing.

3.2 Fluorescenct probes

Fluorescent probes are fluorescently active molecules or parts of the molecules that can be introduced into a system under study to infer information about their environment.

The properties of probes depend on physicochemical properties of the environment, which is usually manifested as solvatochromic shifts, the probes report on changes in their vicinity. In biologically relevant systems, fluorescent probes are usually partially hydrated, and probe-water interactions influence the emission spectra. This sensitivity to interactions with water can be effectively utilized. For instance, in the time-dependent fluorescence shift (TDFS) method, a time evolution of fluorescence due to water reorientation around a probe is used to gain information about the local dynamics in the nearest neighborhood of the probe. As evident from the previous discussion of the Jablonski diagram, in order to fully describe the dynamics of fluorescent probes, it can be often essential to include SO coupling to account for intersystem crossings to the triplet states.

Chapter 4

Ab initio MD with non-adiabatic and SO effects: Implementation and applications (Synopsis of Papers)

In this chapter, I will provide an overview of the accompanying papers. Paper I deals with non-adiabatic effects only using correlated single-reference methods. In Paper II, I explain the implementation of adding the SO couplings to the surface hopping dynamics at CAS-SCF level and provide applications to the dynamics of thiophene and selenophene. A paper describing an extension of this approach to TD-DFT, and two other CIS-like WF methods, ADC(2) and CC2 is currently in preparation. In Paper III and IV, applications to fluorescent probes, Prodan and Laurdan respectively, are provided.

4.1 Paper I

Surface Hopping Dynamics with Correlated Single-Reference Methods: 9H-Adenine as a Case Study

4.1.1 Introduction and methodology

This paper reports an implementation of surface hopping dynamics with correlated single-reference methods, namely coupled cluster to approximated second order[28] (CC2), the algebraic diagrammatic construction scheme to second order[29] (ADC(2)), and the time-dependent density functional theory[30] (TD-DFT) into the program system Newton-X.[26, 31]

The underlying quantum chemical calculations are performed by Turbomole[32] and Gaussian.[33] For this paper, I was only using the interfaces with these programs to perform the MD simulations, but for later work, I have augmented and rewritten large portions of the code in order to allow different multiplicities and SO coupling. The implementation follows the fewest switches approach discussed in Section 2.2. Following Hammes-Schiffer and Tully,[6] the time derivative coupling terms between the states are approximately calculated from the overlaps of the electronic wave functions ψ_k and ψ_l of the states k and l in the consecutive steps $t - \Delta t$ and t,

$$S_{kl}(t) = \langle \psi_k(t - \Delta t) | \psi_k(t) \rangle. \tag{4.1}$$

Details about the calculation of the overlap of the CIS-like wave functions can be found in the paper and references within.

Using linear interpolation, the time derivative coupling terms may be approximated from the overlaps as

$$\langle \psi_k | \frac{\partial}{\partial t} | \psi_l \rangle = \frac{1}{4\Delta t} \left[3S_{kl}(t) - 3S_{lk}(t) - S_{kl}(t - \Delta t) + S_{lk}(t - \Delta t) \right] \tag{4.2}$$

and used in Eq (2.19) to propagate the coefficients and in Eq (2.20) to calculate the hopping probabilities.

The methodology was applied to 9H-Adenine (Fig 4.1), which makes a

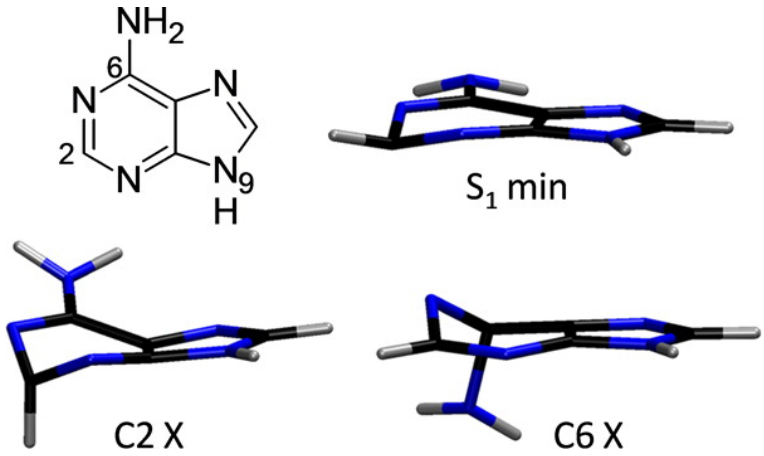

Figure 4.1: 9H-adenine: structural formula, geometries of the S_1 minimum and the C2 and C6 S_1/S_0 conical intersections (X)

good candidate because both experimental and previous theoretical results are available. Simulations based on ab initio methods[34] predicted deactivation via conical intersections characterized by puckering at the C2 atom (see Fig 4.1), while semiempirical simulations[35, 36] predicted that internal conversion happens at a C6-puckered region of the crossing seam. H elimination from an NH bond has also been suggested by some authors.[37]

4.1.2 Main results

Static calculations

Vertical excitation energies Table 4.1 shows vertical excitation energies into the lowest singlet states of 9H-adenine. For all methods, the calculated excitation energies to the $\pi-\pi^*$ states are in an excellent agreement with the experimental result. The combined oscillator strengths of the $\pi-\pi^*$ states are slightly larger than the experimental value. The negative oscillator strength in CC2 reflects the imaginary root arising from the quasi-degeneracy of the states.

	CC2	ADC(2)	TD-DFT	Exp.[38, 39]
$n - \pi^*$	5.08 (0.021)	5.00 (0.026)	5.33 (0.001)	
$\pi - \pi^*$	5.13 (−0.034)	5.06 (0.169)	5.33 (0.280)	5.16 (0.24)
$\pi - \pi^*$	5.16 (0.300)	5.07 (0.101)	5.46 (0.012)	
$\pi - 3s$	5.39 (0.013)	5.39 (0.010)	5.88 (0.006)	

Table 4.1: Vertical excitation energies [eV] and oscillator strenghts

Absorption spectra and initial conditions Simulated absorption spectra for all methods are shown in the top portion of Fig 4.2, together with experimental results from Ref.[39] The CC2 band maximum at 4.95 eV is in excellent agreement with the experimental vapor spectrum (4.92 eV). The ADC(2) maximum is slightly red-shifted (4.87 eV), while the TD-ωB97XD maximum is slightly blue-shifted at 5.09.

For ADC(2), initial conditions for dynamics were sampled using the Wigner distribution from two domains in the simulated spectra: L (low) and M (medium) domains The L-domain is defined as residing in the 4.6 ± 0.1 eV range, whereas the M-domain is defined as residing in the 4.8 ± 0.1 eV range (see bottom part of Figure 2). Out of 3000 initial conditions used to build the spectrum, 218 points are in the L-domain and 407 points are in the M-domain; 50 initial conditions have been selected for the MD simulations using a stochastic algorithm, which also assigned the appropriate initial state.

For TD-DFT, 50 initial conditions have been selected, 30 starting in S_2 and 20 starting in S_3, sampling the entire first spectral band.

Molecular dynamics

ADC(2) vs. CC2 All test trajectories using the CC2 method failed due to numerical problems within the first 100 fs. The problems are caused by the nonsymmetric CC2 Jacobian, which tends to produce imaginary eigenvalues near degenerated excited states. ADC(2) has a symmetric Jacobian with strictly real eigenvalues; hence, it does not suffer from these problems. Therefore, all the trajectories have been calculated using ADC(2) only.

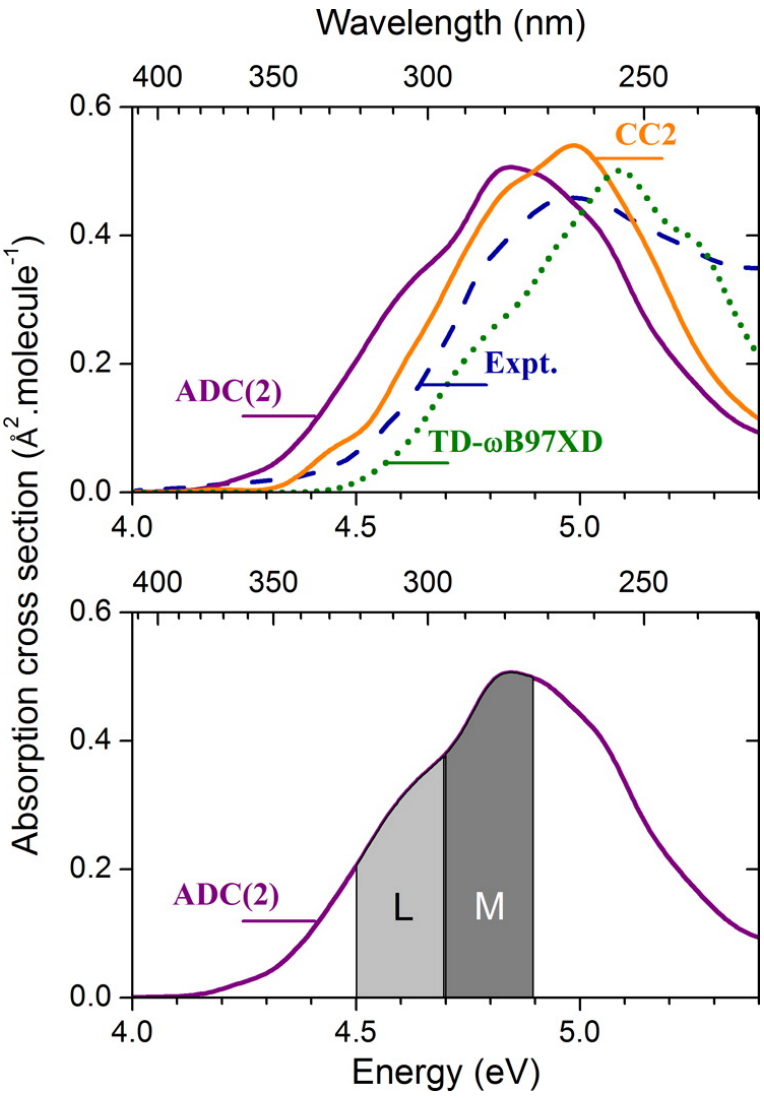

Figure 4.2: Top: Simulated absorption spectrua of 9H-adenine compared with experiment[39] Bottom: ADC(2) spectrum, showing the L (4.6 ± 0.1 eV) and M (4.8 ± 0.1 eV) domains from where initial conditions for the dynamics were selected.

ADC(2) dynamics results Surface hopping trajectories were computed for a maximum of 1000 fs or until an $S_1 - S_0$ energy gap smaller than 0.1 eV was reached. The trajectories employing ADC(2) method were in fact so stable, that when termination criteria are not applied, they continue running with formal negative excitation energies (response state lower than the closed shell) after $S_1 - S_0$ crossings. However, in this area, strong mixing between the closed shell and the excited configurations is to be expected, which is absent in the single reference treatment. Thus, ADC(2), and also TD-DFT (in its linear response formalism based on the adiabatic approximation), CIS and other methods employing a CIS-like wave function cannot correctly describe the region of the $S_1 - S_0$ crossing.

Deactivation mechanism ADC(2) dynamics predicted that conical intersections with C2 deformations are the main deactivation channel in the dynamics starting in the low-energy region of the spectrum. Intersections with C6 deformations are relevant as well, and its importance tends to increase for absorption in the high-energy part of the spectrum. Intersections due to H elimination play only a minor role.

Figure 4.3 shows a comparison of the ADC(2) results with previous computational studies and the experiment. While ADC(2) predicts a slightly lower S_0 population, it is still in a good qualitative agreement with the experiment. The OM2/MRCI method also gives similar results, but it turns out that it underestimates the reaction barrier between the S_1 minimum and the C6-puckered conical intersection compared to higher levels of theory;[40] hence it probably gives the correct populations for an incorrect reason.

Results of TD-DFT dynamics with the ωB97XD functional The paper also presents results for the ωB97XD[41] functional, that was not part of the previous study.[40] Out of 50 trajectories, only six (12 %) returned to ground state within 1 ps, all following the C2 deformations pathway. This is consistent with the previous TD-DFT results for other functionals. The failure of TD-DFT to describe the excited-state dynamics of adenine is related to the DFT overstabilization of the ground-state potential energy along

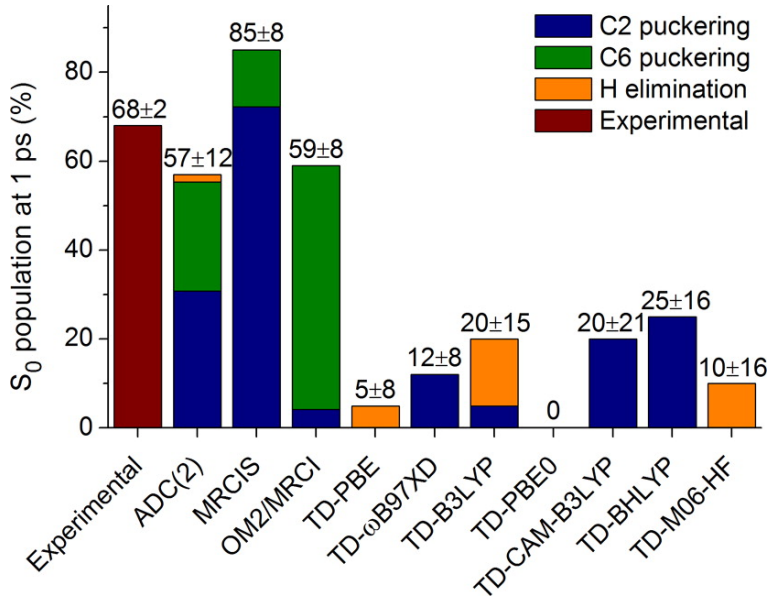

Figure 4.3: Comparison of the present ADC(2) and TD-ωB97XD results for deactivation within 1 ps with the experimental[42] and diverse computational results.[40] (Margins of error estimated for a 90% confidence level).

planar distortions, compared to out-of-plane distortions. This effect creates a bias toward motion with a small degree of puckering, delaying the time to reach the conical intersections.

4.1.3 Conclusions

A new implementation of surface-hopping dynamics in Newton-X using CC2, ADC(2) and TD-DFT was presented. For all cases, non-adiabatic couplings are based on overlaps of formal CIS wave functions. As a common limitation of single-reference methods, these methods are only suitable for simulating dynamical processes that do not require states of strong double-excitation character and occurring within the excited-state manifold until the minimum of the first excited state or a crossing to the ground state is reached. These criteria are often met in various processes including exciton dynamics, energy or electron transfers, excimer formation or excited-state proton transfer; for these applications CC2, ADC(2) or TD-DFT may provide a very viable

alternatives to computationally much more demanding methods, especially in combination with the resolution of the identity (RI) approximation.

As a test case, dynamics of 9H-Adenine in the gas phase was performed. The CC2 method turned out to be unstable in this case because of numerical problems near degenerate excited states caused by a nonsymmetrical Jacobian. ADC(2) on the other hand provided excellent stability and very good performance. The deactivation to the ground state predicted by ADC(2) is qualitatively correct, although somewhat smaller than the experimental result.

Results employing dynamics of TD-DFT with the long-range corrected ωB97XD functional have been published, to our knowledge, for the first time in combination with surface hopping dynamics. Similarly, as with other functionals, ωB97XD also overstabilizes the ground-state potential energy of 9H-Adenine along planar distortions and fails to predict the ultrafast deactivation.

Overall, out of the three methods tested, ADC(2) has the greatest potential as a single-reference method to provide high-level information on nonadiabatic processes involving multiple excited states.

4.2 Paper II

A new approach to molecular dynamics with non-adiabatic and spin-orbit effects with applications to QM/MM simulations of thiophene and selenophene

4.2.1 Introduction and methodology

This paper contains some of the core parts of my work on this project. It describes an implementation of surface hopping dynamics on potential energy surfaces resulting from the spin-orbit splitting, i.e., surfaces corresponding to the eigenstates of the total electronic Hamiltonian including the SO coupling and explains how to handle problems caused by the random phases of degenerate eigenvectors and a possibility of crossings of the resulting mixed states. The methodology is extended with the QM/MM approach and applied to deactivation of excited states of thiophene and selenophene in the gas phase and in solution.

Implementation details As outlined in the previous chapter, we employ Tully's surface hopping molecular dynamics.[4, 5] The code of my implementation is based on previous Newton-X implementation, which I have completely rewritten from Fortran to C++. The new implementation is capable of running the dynamics both on the adiabatic surfaces in the MCH representation and also in the diagonal representation where the surface corresponds to the eigenstates of the total electronic Hamiltonian including the SO coupling. In the latter case, the coefficients are governed by Eq (2.24):

$$\frac{d}{dt}\bar{\boldsymbol{c}} = -(\mathrm{i}\boldsymbol{E}^{\mathrm{tot}} + \dot{\boldsymbol{R}} \cdot \bar{\boldsymbol{K}} + \boldsymbol{U}^{\dagger}\frac{d\boldsymbol{U}}{dt})\bar{\boldsymbol{c}} \equiv \boldsymbol{A}\bar{\boldsymbol{c}} \tag{4.3}$$

As already discussed, the term $d\boldsymbol{U}/dt$ can cause numerical problems that are difficult to overcome. Original phase alignment as proposed by Gonzalez et al.[16] in the initial implementation in the SHARC code[43] turned out to be insufficient and later abandoned for the "3-step propagator" technique,[17]

where the $d\boldsymbol{U}/dt$ term is avoided (see Eq (2.27)).

In this paper, we have proposed an alternative solution. Notice that the transformation matrix $\boldsymbol{U}(t)$ is chosen in each step such that it exactly diagonalizes the total Hamiltonian $\boldsymbol{H}^{\mathrm{tot}}(t)$. If we alleviate this condition and employ a general transformation matrix $\tilde{\boldsymbol{U}}(t)$, we obtain

$$\tilde{c}_i(t) = \sum_j \tilde{U}^*_{ji}(t) c_j(t) \tag{4.4}$$

and

$$\frac{d}{dt}\tilde{\boldsymbol{c}}(t) = -(\mathrm{i}\tilde{\boldsymbol{H}}(t) + \dot{\boldsymbol{R}}(t)\cdot\tilde{\boldsymbol{K}}(t) + \tilde{\boldsymbol{U}}^{\dagger}(t)\frac{d\tilde{\boldsymbol{U}}(t)}{dt})\tilde{\boldsymbol{c}}(t), \tag{4.5}$$

where $\tilde{\boldsymbol{K}}(t) = \tilde{\boldsymbol{U}}^{\dagger}(t)\boldsymbol{K}(t)\tilde{\boldsymbol{U}}(t)$ are the transformed NAD couplings and $\tilde{\boldsymbol{H}}(t) = \tilde{\boldsymbol{U}}^{\dagger}(t)\boldsymbol{H}(t)\tilde{\boldsymbol{U}}(t)$ is the transformed Hamiltonian (not necessarily diagonal). This equation is thus a generalization of (2.24) to arbitrary time-dependent basis given by the transformation matrix $\tilde{\boldsymbol{U}}(t)$.

I have implemented and tested two different approaches based on this general choice of $\tilde{\boldsymbol{U}}(t)$. In the first approach, we take $\tilde{\boldsymbol{U}}(t)$ to be "locally constant", i.e., the same at the beginning and at the end of the current MD step, forcing the derivative to be trivially zero. At the beginning of each time step, we diagonalize $\boldsymbol{H}^{\mathrm{tot}}(t)$ to obtain $\boldsymbol{U}(t)$ and set

$$\begin{aligned} \tilde{\boldsymbol{U}}(t) &= \boldsymbol{U}(t), \\ \tilde{\boldsymbol{U}}(t-\Delta t) &= \boldsymbol{U}(t), \end{aligned} \tag{4.6}$$

which automatically leads to

$$\frac{d\tilde{\boldsymbol{U}}}{dt} = 0. \tag{4.7}$$

The "old" coefficients need to be transformed to the new basis using:

$$\begin{aligned} \tilde{\boldsymbol{c}}(t-\Delta t) &= \tilde{\boldsymbol{U}}^{\dagger}(t-\Delta t)\boldsymbol{c}(t-\Delta t) \\ &= \tilde{\boldsymbol{U}}^{\dagger}(t-\Delta t)\boldsymbol{U}(t-\Delta t)\bar{\boldsymbol{c}}(t-\Delta t) \\ &= \boldsymbol{U}(t)^{\dagger}\boldsymbol{U}(t-\Delta t)\bar{\boldsymbol{c}}(t-\Delta t) \end{aligned} \tag{4.8}$$

and propagated using Eq (4.5). This procedure is repeated in each time step.

In the second approach, we again set $\tilde{\boldsymbol{U}}(t) = \boldsymbol{U}(t)$, but this time we find a transformation of $\boldsymbol{U}(t - \Delta t)$ to $\tilde{\boldsymbol{U}}(t - \Delta t)$ in such a way, that it's overlap with $\boldsymbol{U}(t)$ is close to a unit matrix

$$\tilde{\boldsymbol{U}}^{\dagger}(t - \Delta t)\boldsymbol{U}(t) \to \mathbf{1}, \tag{4.9}$$

thus removing all of the redundant degrees of freedom before computing the finite difference of the $\tilde{U}$ matrix explicitly

$$\frac{d\tilde{\boldsymbol{U}}}{dt}(t - \Delta t/2) = \frac{\tilde{\boldsymbol{U}}(t) - \tilde{\boldsymbol{U}}(t - \Delta t)}{\Delta t}. \tag{4.10}$$

To obtain such transformation of $\boldsymbol{U}(t - \Delta t)$ we use singular value decomposition as detailed in the paper.

Since the $\tilde{\boldsymbol{U}}$ matrix no longer exactly diagonalizes $\boldsymbol{H}^{\mathrm{tot}}(t)$, the more general equation (4.5) has to be employed and the "old" coefficients, the Hamiltonian and non-adiabatic couplings need to be transformed:

$$\begin{aligned}
\tilde{\boldsymbol{c}}(t - \Delta t) &= \tilde{\boldsymbol{U}}^{\dagger}(t - \Delta t)\boldsymbol{c}(t - \Delta t) = \tilde{\boldsymbol{U}}^{\dagger}(t - \Delta t)\boldsymbol{U}(t - \Delta t)\bar{\boldsymbol{c}}(t - \Delta t), \\
\tilde{\boldsymbol{K}}(t - \Delta t) &= \tilde{\boldsymbol{U}}^{\dagger}(t - \Delta t)\boldsymbol{K}(t - \Delta t)\tilde{\boldsymbol{U}}(t - \Delta t), \\
\tilde{\boldsymbol{H}}(t - \Delta t) &= \tilde{\boldsymbol{U}}^{\dagger}(t - \Delta t)\boldsymbol{H}(t - \Delta t)\tilde{\boldsymbol{U}}(t - \Delta t).
\end{aligned} \tag{4.11}$$

The gradients of the eigenvalues E^{tot} used for the nuclear trajectory are obtained as:

$$\begin{aligned}
\nabla_{\mathbf{R}} E_i^{\mathrm{tot}} &= \nabla_{\mathbf{R}} \langle \psi_i | \hat{H}^{\mathrm{tot}} | \psi_i \rangle = \langle \psi_i | \nabla_{\mathbf{R}} \hat{H}^{\mathrm{tot}} | \psi_i \rangle = \sum_{kl} U_{ki}^* U_{li} \langle \phi_k | \nabla_{\mathbf{R}} \hat{H}^{\mathrm{tot}} | \phi_l \rangle \\
&= \sum_{kl} U_{ki}^* U_{li} \langle \phi_k | \nabla_{\mathbf{R}} (\hat{H}^{\mathrm{MCH}} + \hat{H}^{\mathrm{SO}}) | \phi_l \rangle
\end{aligned} \tag{4.12}$$

Since matrix elements of $\nabla_{\mathbf{R}} \hat{H}^{\mathrm{SO}}$ are not available in any present program, we neglect them (which was done in the work of Gonzalez et al.[17] as well). Then one can further simplify the gradient expression (4.12)

$$\langle \phi_k | \nabla_{\mathbf{R}} \hat{H}^{\mathrm{MCH}} | \phi_l \rangle = \delta_{kl} \nabla_{\mathbf{R}} E_k^{\mathrm{MCH}} + (E_l^{\mathrm{MCH}} - E_k^{\mathrm{MCH}}) K_{kl} \tag{4.13}$$

All gradients in the MCH basis as well as NAD couplings thus contribute to the final gradient in the "diagonal basis"

$$\nabla_{\mathbf{R}} E_i^{\mathrm{tot}} = \sum_{kl} U_{ki}^* \left[\delta_{kl} \nabla_{\mathbf{R}} E_k^{\mathrm{MCH}} + (E_l^{\mathrm{MCH}} - E_k^{\mathrm{MCH}}) K_{kl} \right] U_{li} \tag{4.14}$$

The non-adiabatic coupling terms $\boldsymbol{K}$ also contribute to the gradients; if only time-derivative couplings $\dot{\boldsymbol{R}} \cdot \boldsymbol{K}$ are available, this contribution has to be neglected.

The hopping probabilities can be calculated analogously as in the MCH representation: Since this equation features $d\boldsymbol{U}/dt$ explicitly, for the 3-step propagator a different formula derived by Granucci et al.,[44] which can be used for any representation of the Hamiltonian. Here we present it in the form for the diagonal basis as also employed by Gonzalez et al.:[17]

$$p(k \to j) = \left(\max \left\{ 1 - \frac{|\bar{\mathrm{c}}_{\mathrm{k}}(\mathrm{t} + \Delta \mathrm{t})|^2}{|\bar{\mathrm{c}}_{\mathrm{k}}(\mathrm{t})|^2}, 0 \right\} \right) \frac{\Re \left[\bar{c}_j(t + \Delta t) \bar{A}_{jk}^* \bar{c}_k^*(t) \right]}{|\bar{c}_k(t)|^2 - \Re \left[\bar{c}_k(t + \Delta t) \bar{A}_{kk}^* \bar{c}_k^*(t) \right]} \tag{4.15}$$

where $\bar{A}_{jk}$ are matrix elements of the coefficient propagator in the diagonal basis

$$\bar{\boldsymbol{c}}(t + \Delta t) = \bar{\boldsymbol{A}}(t + \Delta t, t) \bar{\boldsymbol{c}}(t) \tag{4.16}$$

and negative $p(k \to j)$ probabilities as well as $p(k \to k)$ are set to zero.

Applications The described methodology is first tested on a simple model system, consisting of two harmonic oscillators coupled by a constant off-diagonal term.

The second presented application is the ultrafast deactivation of thiophene and selenophene in the gas phase, in the ethanol solvent and in bulk liquid phase; here the energies, gradients, non-adiabatic and spin-orbit coupling have been calculated on the state-averaged CASSCF level in Molpro,[45] using the active space of 8 electrons in 7 orbitals. The Breit-Pauli Hamiltonian was used for spin-orbit coupling. Up to five singlet states and up to five triplet states have been included with equal weights in the state-averaging procedure. For comparison, dynamics on singlet states only has also been

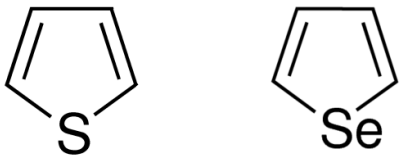

(A) (B)

Figure 4.4: Structural formula of thiophene (A) and selenophene (B)

computed. Calculations in the liquid phase have been carried out using the QM/MM approach,[25] where the MM part has been calculated using general Amber force field (GAFF)[46] by Gromacs.[47]

4.2.2 Main results

Deactivation of thiophene and selenophene

Molecular dynamics without SO couplings First, the dynamics in the singlet manifold has been performed for both thiophene and selenophene starting in both S_1 and S_2 states. Deactivation after S_1 excitation is relatively slow, making running many trajectories computationally expensive; hence we decided to limit the investigation to the S_2 excitation only. 100 trajectories have been calculated for both thiophene and selenophene. The resulting averaged state populations are depicted in Fig 4.5. The S_2 state population first quickly decays to the S_1 state via a first conical intersection; this is followed by a slower decay from the S_1 state to the ground state S_0.

MD including SO couplings A subset of 32 initial conditions from the previous trajectories was recalculated with spin-orbit coupling utilizing all 3 approaches implemented in Newton-X as discussed in the previous section: the 3-step propagator and two new "one-step" approaches. For comparison, the same set of trajectories has been recalculated with SHARC as well.

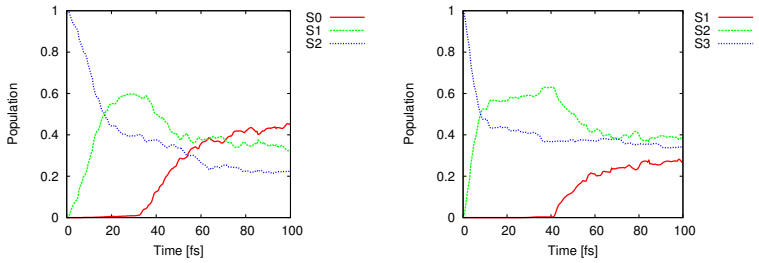

Figure 4.5: Evolution of average populations in thiophene (left) and selenophene (right) without SO, averaged over 100 trajectories initiated in the S_2 state

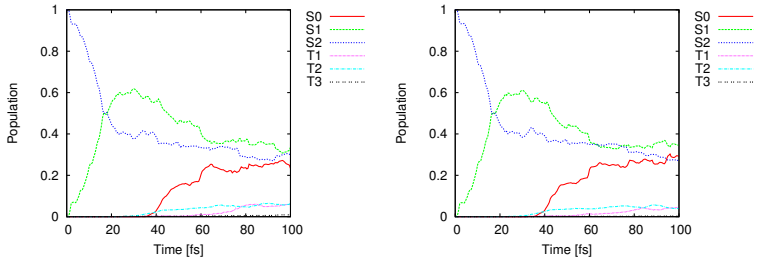

Figure 4.6: Evolution of average populations of thiophene calculated by Newton-X (left) and SHARC (right) with SO couplings included

Thiophene The population transfer to the triplet states in thiophene is low. All 3 approaches implemented in Newton-X produced identical populations, results obtained by SHARC were almost identical as well, as seen in Fig 4.6.

Selenophene In the case of selenophene, the influence of the triplet states is higher due to greater spin-orbit coupling (see Fig 4.7 left) reaching about 40 % after about 80 fs. Evolution of energies along a sample trajectory is shown in Fig 4.7 right.

Deactivation mechanism The mechanism of the deactivation proceeds via the ring opening pathway for both thiophene and selenophene. Fig 4.8 illustrates this for the example of thiophene by showing the plot of the ring

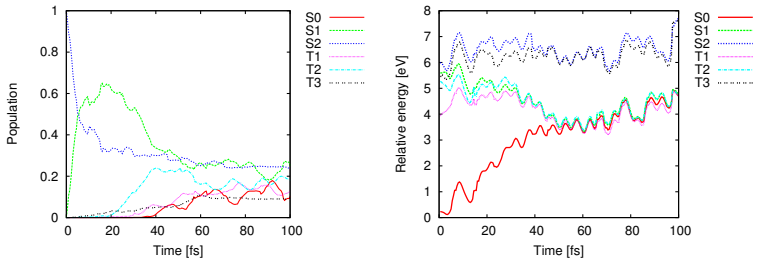

Figure 4.7: Evolution of average state populations for an ensemble of trajectories (left) and energies obtained along an example trajectory (right) for selenophene in the gas phase

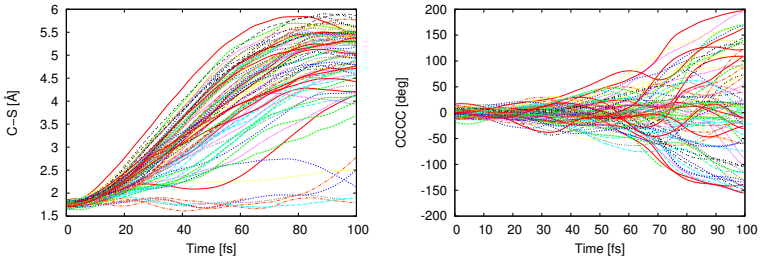

Figure 4.8: Evolution of geometrical parameters describing the ring opening: CS distance (left) and CCCC dihedral angle (right).

opening S-C coordinate for all trajectories. There are, of course, two S-C bonds, so only the one that reached the largest value during the trajectory is plotted. The ring opening initiates in the molecular plane, followed by an out-of-plane rotation of the CCCC dihedral angle shown in the right panel of Fig 4.8.

Comparing with the previously shown figures, we observe that the ring opening happens before the triplet states are populated; hence the mechanism is not strongly influenced.

Simulations in the liquid phase Simulations in the liquid phase have been performed using the QM/MM approach. 50 trajectories have been calculated for both thiophene and selenophene in both ethanol solvent and bulk liquid phase. In all cases, the deactivation is slowed down slightly,

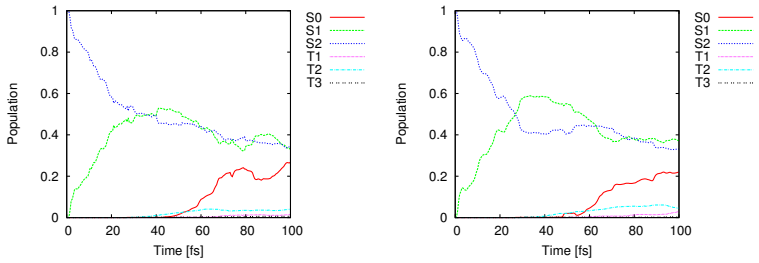

Figure 4.9: Evolution of average populations of thiophene in ethanole (left) and bulk liquid phase (right)

but the overall picture remained unchanged. As an example, in Fig 4.9, the populations obtained for thiophene in the ethanol solvent and bulk thiophene liquid are shown, very similar to the populations obtained in the gas phase (Fig 4.6).

The mechanism of the deactivation also remained unchanged, with a slight difference that the out-of-plane motion was somewhat reduced, as may be expected, as the motion of the molecule in the QM region is partially sterically hindered by the surrounding molecules.

4.2.3 Conclucions

Non-adiabatic dynamics on the surfaces resulting from splitting induced by the spin-orbit coupling has been implemented to Newton-X. The electronic wave function propagation is achieved utilizing 3 different approaches: i) with an explicit calculation of the $\boldsymbol{U}$ derivative using SVD alignment, ii) the locally constant $\boldsymbol{U}$ representation and iii) the 3-step integrator approach. The implementation also allows including the environment via the QM/MM approach.

The methodology was tested on model systems and employed to investigate the ultrafast deactivation of thiophene and selenophene upon excitation to the S_2 state. For thiophene, the resulting deactivation lifetime of the S_2 state was 68 fs in the gas phase, 76 fs in ethanol solution and 78 fs in the liquid phase, in a good agreement with the experimental value of 80 fs (liquid

phase). For selenophene, the obtained S_2 lifetime was 60 fs in the gas phase and 62 fs for both ethanol solution and liquid phase. For both molecules, the deactivation of the S_2 state proceeds via the ring opening pathway. The total population of triplet states reaches around 15 % and 40 % after 80 fs for thiophene and selenophene respectively, but the triplet states are populated only after the ring opening is initiated; hence the triplet states do not directly contribute to the deactivation mechanism.

4.3 Paper III

Fluorescence of PRODAN in water: A computational QM/MM MD study

4.3.1 Introduction and methodology

Prodan (6-propionyl-2-dimethylaminonaphthalene (see Fig 4.10A) is a fluorescent probe often used in time-dependent solvent-relaxation studies of hydrated lipid membranes,[48, 49] because of a strong dependence of it's emission spectra on the solvation state. Despite the extensive use of Prodan in fluorescent studies, its excited state properties including the geometry of the emitting state are not fully resolved. Two conformers of the intramolecular charge transfer state have been proposed: planar and twisted (Fig 4.10B and C). Furthermore, none of the previous computational studies of Prodan fluorescence reproduces the extent of the solvatochromic shift in water.

In this paper, the influence of the water environment on Prodan in the excited state is directly studied by means of the QM/MM scheme introduced in section 2.4. Either Prodan or Prodan with several water molecules is treated at the TD-DFT[30] level, whereas a molecular mechanics model is employed to account for an extended water environment.

Excited state TD-DFT MD in the gas phase Excited state molecular dynamics of Prodan in the S_1 state is performed at the TD-DFT level of theory [20]. The BHLYP functional[50] is employed, while PBE0[51] and B3LYP[52] functionals were tested. The def2-SVP basis set is used.[53] The dynamics is carried out in Newton-X extended with a new interface I have written for Gromacs.

Bechmark calculations To select the appropriate functional, a benchmark calculation using a completely renormalized equation-of-motion coupled cluster method with singles, doubles and noniterative triples[54] CR-EOM-CCSD(T) has been performed at the Chinook supercluster system at

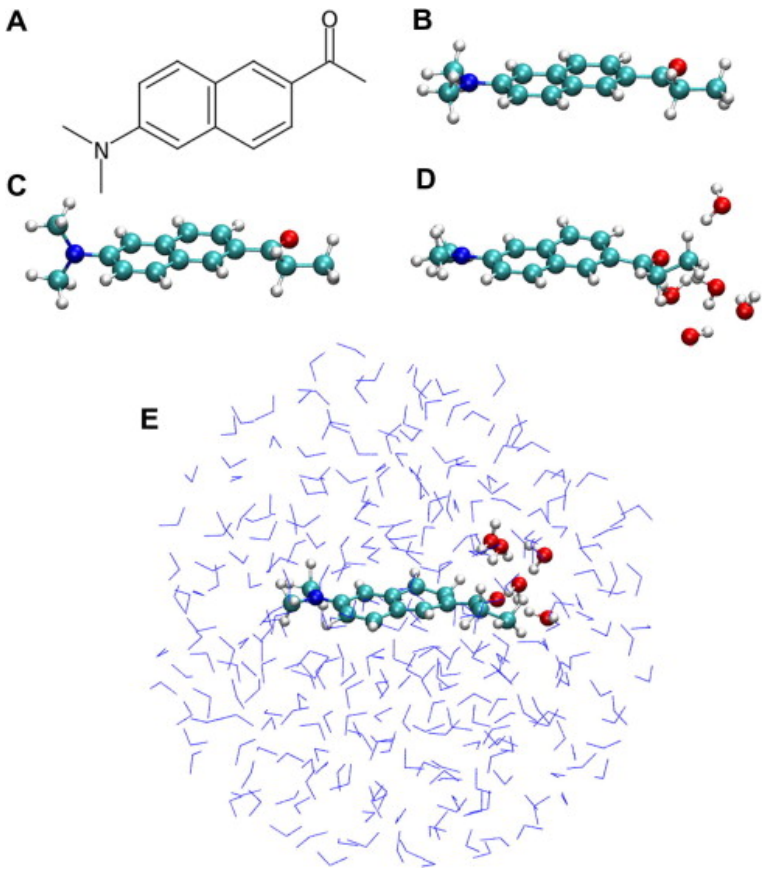

Figure 4.10: Prodan: structural formula (A), geometries of the planar (B) and twisted (C) conformers, structure including 5 QM water molecules (D), structure including 5 QM and 295 MM water molecules E

the Pacific Northwest National Laboratory.

Excited state simulations in the water environment Several computational schemes have been employed:

1. Prodan + 5QM WAT To account for solutesolvent hydrogen bonds between carbonyl oxygen atom of Prodan and water, TD-DFT/BHLYP MD trajectories were calculated for clusters consisting of Prodan with five water molecules in the proximity of the carbonyl oxygen atom.

2. Prodan + 300MM WAT In this scheme 300 explicit water molecules are included by means of the QM/MM method

3. Prodan + 5QM + 295MM WAT This scheme combines 295 water molecules in the MM region and 5 water molecules in the QM region.

Polarization effects To include polarization effects, the AMOEBA forcefield was employed. The classical point dipole moment is induced at each polarizable atomic site according to the electric field created by multipoles of the all remaining charged sites. Molecular polarization is achieved via mutual induction in a self-consistent manner. It is not straightforward to employ the polarization in the simple subtractive scheme introduced in section 2.4. I have developed a simple approximate scheme to use AMOEBA within our QM/MM implementation in Newton-X.

1. The QM region with MM charges embedded into the QM Hamiltonian (QM region is polarized by the environment, MM-MM electrostatics is not calculated)

2. The whole system is calculated at the MM level using the polarizable AMOEBA force field including induced dipoles. This step includes polarization of the solvent but includes unwanted QM-QM and QM-MM interactions that are now double-counted.

3. The whole system is recalculated again at the MM level employing simple point charges and subtracted. This eliminates the double counting included in step 2 but also removes MM-MM interactions.

	B3LYP	PBE0	BHLYP	CR-EOM-CCSD(T)
$E_{\text{twisted}} - E_{\text{planar}}$	-7.2	-4.5	13	14
$E_{\text{planar}}(S_1 \rightarrow S_0)$	3.26 (0.20)	3.36 (0.20)	3.72 (0.24)	3.43
$E_{\text{twisted}}(S_1 \rightarrow S_0)$	2.35 (3×10^{-4})	2.51 (3×10^{-4})	3.77 (5×10^{-4})	3.58

Table 4.2: Relative stability of Prodan conformers [kcal/mol] and vertical emission energies [eV]. Values of oscillator strength are given in parenthesis.

4. MM region is calculated to add the missing MM-MM interactions once again.

4.3.2 Main results

Stability of the conformers The relative stability of the conformers of Prodan was calculated (see Table 4.2). In both B3LYP and PBE0 the twisted conformer has lower energy (by 7.2 and 4.5 kcal/mol, accordingly), such stabilization of the twisted geometry is artificial, resulting from overstabilization of charge transfer states by some of DFT functionals. In CR-EOM-CCSD(T), the planar conformer is more stable by 14.0 kcal/mol, which is well reproduced by the BHLYP functional (13.0 kcal/mol), which was hence chosen for the examination of excited state properties of Prodan in the rest of the paper.

Simulated emission spectra

Gas phase results In Fig 4.11, gas phase emission spectra of Prodan obtained from MD trajectories in the S_1 state at TD-DFT/BHLYP level are presented and compared with the experimental fluorescence spectrum in water. The values of vertical transition energies calculated for the optimized twisted and planar conformers are marked with bars. The emission band is centered around 3.7 eV for both conformers. The twisted conformer is not stable in the gas phase trajectories and undergoes planarization within 50 fs.

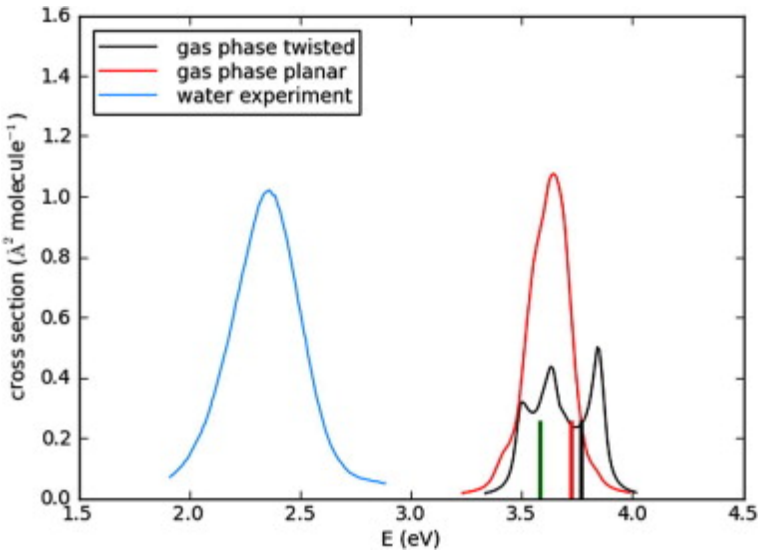

Figure 4.11: Simulated fluorescence spectra of Prodan in the gas phase compared with the experimental spectrum measured in water (in arbitrary units). Vertical transition energies are shown for the twisted (black bar) and planar (red bar) conformers in the gas phase. For COSMO, both energies are almost equal (green bar)

Geometry	Gas phase	COSMO
$E_{\text{planar}}(S_1 \rightarrow S_0)$	3.72 (0.24)	3.58 (0.34)
$E_{\text{twisted}}(S_1 \rightarrow S_0)$	3.77 (5×10^{-4})	3.59 (6×10^{-4})

Table 4.3: Comparison of vertical emission energies [eV] in the gas phase and using COSMO. Values of oscillator strength are given in parenthesis.

Continuum solvation model As a first step to approximately account for the influence of water, we employed the COSMO continuum solvation model.[55] In Table 4.3, the results obtained with COSMO are presented (the emission energy predicted by COSMO is also shown in Fig 4.11). For both planar and twisted conformers, the emission energy only slightly reduced with respect to the gas phase (0.14 and 0.18 eV for the planar and the twisted case). Hence, the continuum solvation model is not able to describe the influence of the water environment on Prodan emission. This is in accord with the previous studies where continuum solvation models are shown to reproduce about 0.2 eV of the Prodan red shift in water.

Explicit-water models

Prodan + 5 QM WAT Including 5 explicit water molecules in the vicinity of the carboxyl group into the simulation leads to a red shift of about 0.2 eV. Similarly as in the gas phase, a planarization of the twisted conformer occurred on the timescale below 100 fs.

Prodan + 300 MM WAT In the second computational scheme including explicit water, Prodan and 300 water molecules are simulated using the QM/MM approach. The emission bands calculated employing non-polarizable water models are located in the energy range of 2.6 – 4.0 eV with maxima at 3.35 eV, and are blue-shifted with respect to the experiment by about 1.0 eV. The twisted conformer is stable during the whole trajectory (over 1500 fs), however, the low intensity of the peaks is not sufficient to explain the experimental results.

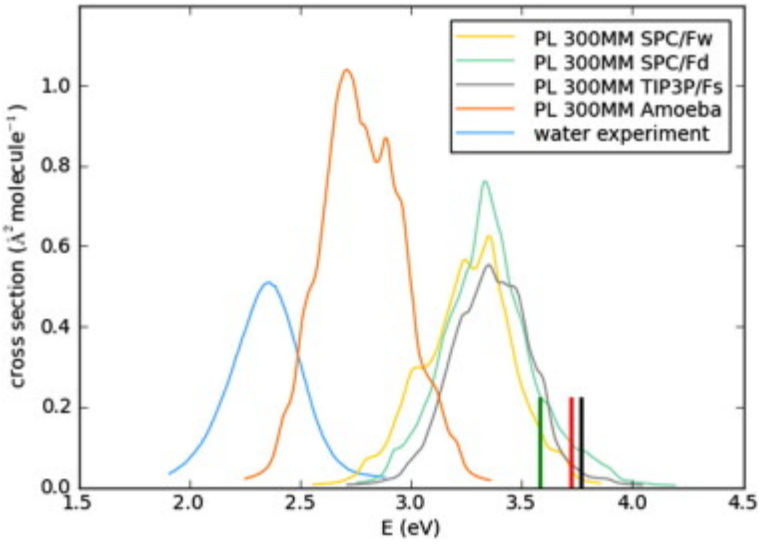

Figure 4.12: Simlated fluorescence spectra of the planar conformer of Prodan in water using the QM/MM scheme Prodan + 300MM WAT with various classical water models. The experimental spectrum in water (in arbitrary units) and energies of vertical transitions are shown for comparison (see Fig 4.11)

Prodan + 5 QM + 295 MM WAT To estimate the influence of implicit solvent molecules in the QM subsystem and to account for part of the polarization effects, we reassigned five waters from the MM region to the QM one in the QM/MM scheme. The inclusion of five waters in the QM region leads to 0.1 up to 0.2 eV emission energy red shift, depending on the force field employed for MM water.

Polarization effects Polarization effects have been included using the Amoeba force field. The spectrum for the planar conformer is located between 2.2 and 3.4 eV with the maximum at 2.7 eV. Hence, polarization causes approximately 0.65 eV red shift, and the spectrum obtained with water polarization included is blue-shifted with regard to the experimental by only 0.35 eV.

4.3.3 Conclusions

The influence of water on the emission spectrum of Prodan is investigated at the TD-DFT level of theory. Based on a CR-EOM-CCSD(T) benchmark, BHLYP functional was selected for the study.

Static gas phase $S_1 \rightarrow S_0$ transition energy is blue-shifted by 1.4 eV with regard to the experiment in water. Spectra generated based on MD simulations in the gas phase exhibit similar 1.3 eV blue shift. COSMO continuum solvation model corrects the gas phase results by only 0.2 eV.

Explicit water solvent was introduced into the simulations using various computational schemes. Including 5 water molecules into the TD-DFT calculation and including 300 water molecules using the QM/MM approach with standard non-polarizable forcefield only provided a modest improvement over the gas phase results.

Best agreement with the experiment was obtained when polarizable AMOEBA forcefield has been employed. The emission band was significantly, by 1.0 eV, redshifted with respect to the gas-phase calculations, with its maximum was located at 2.7 eV, in quite good agreement with the experimental value of 2.35 eV. It demonstrates that solvent polarization effects are crucial for a proper description of excited state Prodan in water. We estimate that polarization effects account for 0.65 eV emission blue shift in water.

The present results show that the twisted S_1 Prodan conformer is stable in water. Due to its low emission intensity, it cannot effectively contribute to the emission spectrum in water. No transitions between the conformers have been observed on the time scale of 1500 fs which suggests that the associated free-energy barrier is probably relatively high. These conclusions are important for biophysical fluorescent techniques employing Prodan or its derivatives as fluorescent probes, as those methods are based on the influence of the probe's environment on its spectral properties.

4.4 Paper IV

Orientation of Laurdan in Phospholipid Bilayers Influences Its Fluorescence: Quantum Mechanics and Classical Molecular Dynamics Study

4.4.1 Introduction and methodology

In this paper, another fluorescent probes, Laurdan, is investigated. The structure of Laurdan (Fig 4.13) features a long hydrophobic alkyl chain and a fluorophore identical to Prodan. Laurdan is one of the most commonly used probe for the measurements of lipid phase behavior.[56, 57] In particular, the generalized polarization method[58] is frequently used to assess the fluidity of lipid membranes based on the different behavior of Laurdan emission indioleoylphosphatidylcholine (DOPC) and dipalmitoylphosphatidylcholine (DPPC) bilayers.

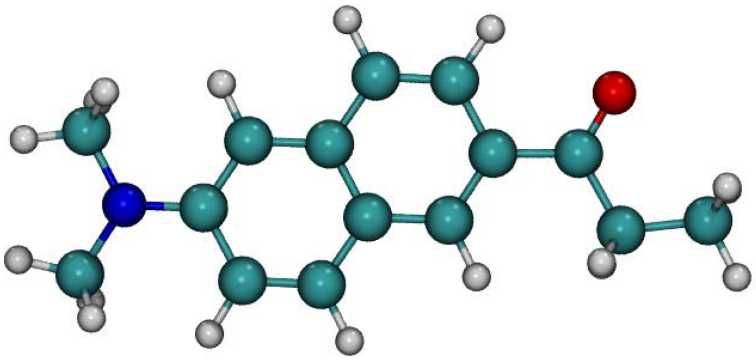

Figure 4.13: Optimized structure of Laurdan fluorophore in in the ground state

Classical MD and both static and dynamic calculations at TD-DFT levels are employed to simulate Laurdan at various timescales. Classical simulations allow us to model Laurdan embedded in the biomembrane for tens of nanoseconds, while TD-DFT dynamics can be used to study the emission processes in the excited state.

Classical MD In the classical MD simulations, a single Laurdan molecule is incorporated in the DOPC and DPPC lipids bilayer each consisting of 128 lipids. Force field parameters for Laurdan were derived based on the GAFF forcefield[46] supplemented with the RESP pointcharges obtained from TD-DFT for Laurdan int the S_0 and S_1 state respectively, while Slipids force field[59] was used for the lipids together with TIP3P water.[60] Polarization effects were additionally considered by using Drude/SWM4-NPD force field[61] for water in case of S_1.

MD trajectories were calculated using Gromacs[47] with typical parameters for membrane MD: 1 bar pressure and temperature of 305 K, employing periodic boundary conditions with PME for long-range electrostatics.

For the S_0 state, trajectories of 1000 nanoseconds were calculated in both DOPC and DPPC membranes. For the S_1 state, 20 trajectories of 10 ns length were calculated for each membrane, starting from snapshots taken from the S_0 MD trajectories.

TD-DFT calculations and QM/MM MD First, B3-LYP[52] and PBE0[51] functionals were benchmarked with cc-pVDZ, cc-pVTZ, aug-cc-pVDZ, and aug-cc-pVTZ basis sets. To approximately include water and cyclohexane environments, COSMO continuum model[55] of solvent was employed. For the QM/MM MD simulations the PBE0 functional with the cc-pVDZ basis was selected. All electronic structure calculations were performed using TURBOMOLE[32] code. The QM/MM simulations are performed using my interface of Newton-X with Gromacs which allows using 2D periodic boundary conditions necessary for membrane calculations.

Calculation of the spectra To calculate the spectra, the line broadening method[62] was used. For calculation of the absorption spectra in the membranes, QM/MM trajectories have been calculated with initial condition based on 30 snapshots taken the from classical MD trajectories in the ground state, sampling the different orientations and incorporation depths of Laurdan in the membranes. From these QM/MM trajectories, several hundreds of random points were selected and used to calculate the absorption

spectrum. The emission spectra were based on geometries obtained from the classical simulations including the polarized water model.

4.4.2 Main results

Static calculations We have revisited the selection of the functional compared to the previous paper. Since the importance of the twisted conformer has been excluded, we decided to further benchmark the B3-LYP and PBE0 functionals that provide better overall agreement with the experimental results. Absorption spectra of the fluorophore in the gas phase have been calculated including 5 singlet excited states. Furthermore, water and cyclohexane solvent have been added using the COSMO model.

The resulting absorption spectra are shown in Fig 4.14 compared to experiment.[63] The agreement is satisfactory; the experimentally observed shoulder building up above 400 nm in the polar water environment with respect to nonpolar cyclohexane is reflected in the calculated spectra as a shift toward higher wavelengths while going from gas phase through nonpolar cyclohexane to water.

Absorption spectra in the membranes Absorption spectra calculated based on the data obtained from the QM/MM MD trajectories of Laurdan in DOPC and DPPC bilayers are shown in Fig 4.15 compared with experimental spectra. There is no significant difference between the membranes in both the experimental and calculated spectra, there are, however, significant differences in the penetration depth and tilt angle of the probe as discussed in the manuscript.

Emission spectra in the membranes In Fig 4.16 the calculated emission spectra are compared to spectra obtained experimentally. Although there is no agreement between absolute positions of the bands, the overall blue shift of the simulated spectra can be expected due to lack of polarization effects and hydrogen bonds as we have seen for the case of Prodan in the previous paper.

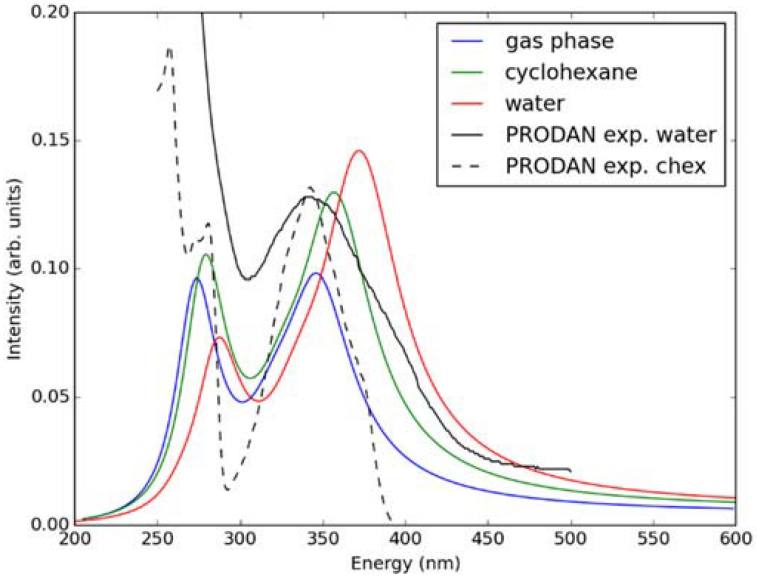

Figure 4.14: Simulated and experimental[63] absorption spectra of the fluorophore of Laurdan/Prodan

Several qualitative conclusions can be made from a comparison of the spectra obtained in DOPC and DPPC. In both the experiment and the simulated spectra, the bands originate in the same energy. In the experiment, however, the DOPC band maximum is redshifted. The key difference between the simulated spectra is the secondary high-wavelength band around 450 nm in DOPC. This band can be directly related to the experimental red shift between DPPC and DOPC.

It is hard to pinpoint precisely why the change in the shape of the peak going from DPPC to DOPC is so small compared to the experiment. In my opinion, the main reasons could be: i) the neglected effects of the environment are slightly different for the membranes; ii) the MM description of the S_1 state is not perfect. Since the S_0 and S_1 states share the same forcefield parameters except of charges, it can be expected that the differences between S_0 and S_1 dynamics will be limited; iii) the QM description of the excited state is generally less accurate than for the ground state, TD-DFT may not be able to describe the differences caused by the environment correctly.

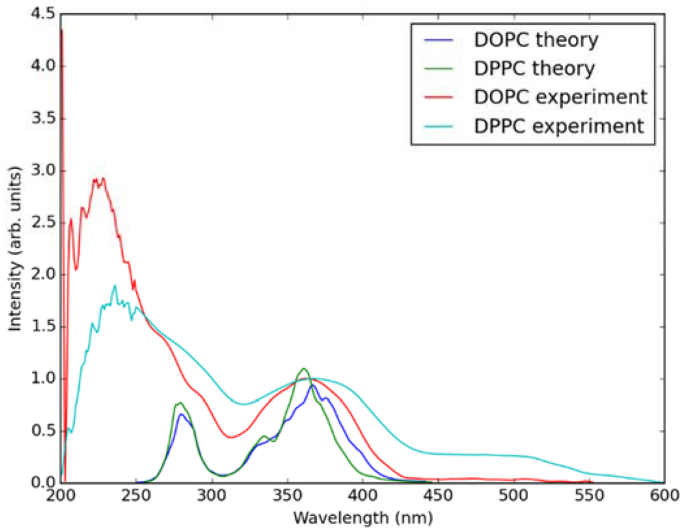

Figure 4.15: Simulated and experimentally measured absorption spectra of Laurdan in DOPC and DPPC membranes

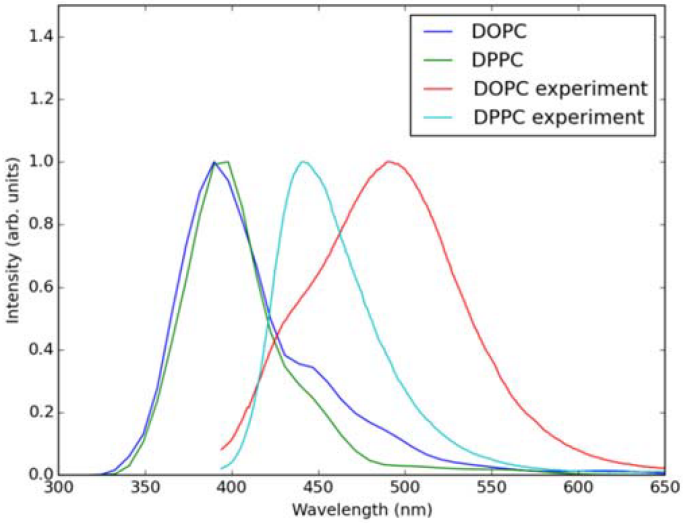

Figure 4.16: Simulated and experimentally measured emission spectra of Laurdan in DOPC and DPPC membranes

The results could be improved by QM/MM dynamics in the S_1 state, possibly also including parts of the surrounding into the QM subsystem. These calculations would be, however, expensive and since the qualitative

agreement has been already achieved, we decided not to perform further QM calculations at this point and analyze the origin of the high-energy band in the DPPC spectrum. subparagraphThe origin of the high-energy band We analyzed in detail the dependence of the emission parameters on the fluorophore depth and orientation in lipid membranes. The data indicate that the highwavelength configurations occur for deep and less tilted fluorophore. Hence, the differences in orientation of Laurdan in the more fluid DOPC and more rigid DPPC can be responsible for differences observed in the respective emission spectra.

4.4.3 Conclusions

The fluorescent probe Laurdan has been investigated in DOPC and DPPC bilayers using both classical MD simulations and TD-DFT MD with the environment included via the QM/MM approach. Absorption and emission spectra of Laurdan for both bilayers have been simulated and compared with experimental measurements.

Based on simulations in both membranes, absorption of Laurdan is not influenced by its environment. This is in agreement with previous results of Prodan and other fluorescent probes sharing a similar fluorophore.

On the other hand, emission properties of Laurdan in lipid bilayers are influenced by the orientation of the probe and depth of membrane penetration. Laurdan fluorophore can not only attain conformations nearly parallel to bilayer normal but can also undergo significant conformational changes including almost complete reversal of the fluorescent moiety toward the membrane interior. This significant orientational variability of Laurdan is important for the analysis of fluorescence experiments.

Chapter 5

Conclusions and Outlook

This thesis describes development and applications of methods of ab initio dynamics simulations with non-adiabatic and spin-orbit effects applicable to accurate simulations of various molecular systems including fluorescent probes in the complex environment of biomembranes.

In the initial parts of the work, only non-adiabatic interactions have been considered. In Paper I, non-adiabatic MD of 9H-adenine is studied using various single reference methods. The study indicated that CC2 and TD-DFT were not suitable in this case while the ADC(2) method provided very reliable results.

In the main part of the project, I have implemented SO coupling to Tullys surface hopping method to Newton-X program package. My implementation allows propagation of the coefficients both in the representation of spin-free Hamiltonian using the 3-step propagator approach as well as directly in the representations of the mixed states using two other approaches: Direct calculation of the $\boldsymbol{U}$ matrix derivative and using a "locally diagonal" representation, where the $\boldsymbol{U}$ matrix is kept constant during the integration.

The implementation can work with various quantum chemical methods. For Paper II, I have developed an interface with Molpro package, which was previously not supported by Newton-X. Recently I have extended the code to work with dynamics on TD-DFT, CC2 and ACD(2) level of theory using Turbomole, where the SO couplings are calculated by an external program by Mojmir Kyvala using the CIS-like wave functions obtained from the response

functions generated by Turbomole.

The representation of spin-mixed states is preferable for the dynamics, but it has a drawback, that in principle all MCH gradients are needed in each step, which significantly increases the computational cost. To address this issue, I have developed a gradient selection routine, which selects the gradients to be calculated based on the current composition of the active state and approximates the skipped gradients. This approach significantly reduces the number of gradients calculated and allows adding additional states to the dynamics at minimal cost.

In parallel with the implementation of surface hopping MD with SO coupling, I have worked on other aspects necessary for simulations of fluorescent probes. I have carried out simulations of Prodan in the gas phase and in water using the QM/MM approach, discussed in Paper III, for which I have also developed an interface of Newton-X with Gromacs that allows planar periodic boundary conditions suitable for calculations of biomembranes. This possibility was subsequently used in Paper IV, where Laurdan was investigated in both DOPC and DPPC membranes.

Further applications inluded 2,4-dithiothymine and 2-thiouracyl. We have also performed simulations of a fluorescent probe Bodipy using MD with both non-adiabatic and spin-orbit couplings to investigate the intersystem crossing crucial for potential uses of Bodipy in photodynamic therapy.

I believe my implementation of surface hopping dynamics with non-adiabatic and SO couplings, combined with the program by Mojmir Kyvala for calculations of SO couplings, is currently the state-of-the-art tool for simulations of fluorescent probes and I hope it will be useful for many more important applications in the future.

Bibliography

[1] D. J. Tildesley M. P. Allen. *Computer Simulation of Liquids*. Oxford University Press, 1987.

[2] D. Frenkel and B. Smit. *Understanding Molecular Simulation: From Algorithms to Applications*. Computational Science Series 1. Academic Press, 2nd edition, 2002.

[3] X. Li, J. C. Tully, H. B. Schlegel, and M. J. Frisch. Ab initio Ehrenfest dynamics. *J. Chem. Phys.*, 123:084106, 2005.

[4] M. Barbatti. Nonadiabatic dynamics with trajectory surface hopping method. *WIREs: Comput. Mol. Sci.*, 1:620, 2011.

[5] J. C. Tully. Molecular dynamics with electronic transitions. *J. Chem. Phys.*, 93:1061, 1990.

[6] S. Hammes-Schiffer and J. C. Tully. Proton transfer in solution: Molecular dynamics with quantum transitions. *J. Chem. Phys.*, 101:4657, 1994.

[7] B. Fu, B. C. Shepler, and J. M. Bowman. Three-state trajectory surface hopping studies of the photodissociation dynamics of formaldehyde on ab initio potential energy surfaces. *J. Am. Chem. Soc.*, 133:7957, 2011.

[8] B. Han and Y. Zheng. Nonadiabatic quantum dynamics in $O(^3P)+H_2 \rightarrow OH+H$: A revisited study. *J. Comput. Chem.*, 32:3520, 2011.

[9] E. Abrahamsson, S. Andersson, N. Marković, and G. Nyman. Dynamics of the O + CN reaction and N + CO scattering on two coupled surfaces. *J. Phys. Chem. A*, 113:14824, 2009.

[10] B. Li and K.-L. Han. Mixed quantum-classical study of nonadiabatic dynamics in the $O(^3P_{2,1,0}, ^1D_2)$ + H_2 reaction. *J. Phys. Chem. A*, 113:10189, 2009.

[11] W. Hu, G. Lendvay, B. Maiti, and G. C. Schatz. Trajectory surface hopping study of the $O(^3P)$ + ethylene reaction dynamics. *J. Phys. Chem. A*, 112:2093, 2008.

[12] T. Takayanagi. Quantum scattering calculations of the $O(^1D)$ + $N_2(X^1\Sigma_g^+)$ $\rightarrow$ $O(^3P)$ + $N_2(X^1\Sigma_g^+)$ spin-forbidden electronic quenching collision. *J. Phys. Chem. A*, 106:4914, 2002.

[13] Y. Amatatsu, K. Morokuma, and S. Yabushita. The resonance Raman spectrum of CH_3I: An application of the MCTDH approach. *J. Chem. Phys.*, 94:4858, 1991.

[14] G. Cui and W. Thiel. Generalized trajectory surface-hopping method for internal conversion and intersystem crossing. *J. Chem. Phys.*, 141:124101, 2014.

[15] G. Granucci, M. Persico, and G. Spighi. Surface hopping trajectory simulations with spin-orbit and dynamical couplings. *J. Chem. Phys.*, 137:22A501, 2012.

[16] M. Richter, P. Marquetand, J. González-Vázquez, I. Sola, and L. González. SHARC: Ab initio molecular dynamics with surface hopping in the adiabatic representation including arbitrary couplings. *J. Chem. Theory Comput.*, 7:1253, 2011.

[17] S. Mai, P. Marquetand, and L. González. A general method to describe intersystem crossing dynamics in trajectory surface hopping. *Int. J. Quant. Chem.*, 115:1215, 2015.

[18] M. Persico and G. Granucci. An overview of nonadiabatic dynamics simulations methods, with focus on the direct approach versus the fitting of potential energy surfaces. *Theor. Chem. Acc.*, 133:1526, 2014.

[19] B. F. E. Curchod, C. Rauer, P. Marquetand, L. González, and T. J. Martínez. Communication: Gaims-generalized ab initio multiple spawning for both internal conversion and intersystem crossing processes. *J. Chem. Phys.*, 144:101102, 2016.

[20] D. A. Fedorov, S. R. Pruitt, K. Keipert, M. S. Gordon, and S. A. Varganov. Ab initio multiple spawning method for intersystem crossing dynamics: Spin-forbidden transitions between $^3B_1$ and $^1A_1$ states of GeH_2. *J. Phys. Chem. A*, 120:2911, 2016.

[21] R. R. Zaari and S. A. Varganov. Nonadiabatic transition state theory and trajectory surface hopping dynamics: Intersystem crossing between $^3B_1$ and $^1A_1$ states of SiH_2. *J. Phys. Chem. A*, 119:1332, 2015.

[22] D. Bakowies and W. Thiel. Hybrid models for combined quantum mechanical and molecular mechanical approaches. *J. Phys. Chem.*, 100:10580, 1996.

[23] P. Sherwood. *Hybrid Quantum Mechanics/Molecular Mechanics Approaches*, volume 3 of *NIC Series*, page 285. John von Neumann Institute of Computing, Jülich, 2000.

[24] H Lin and D. G. Truhlar. QM/MM: What have we learned, where are we, and where do we go from here? *Theor. Chem. Acc.*, 117:185, 2006.

[25] M. Ruckenbauer, M. Barbatti, T. Mueller, and H. Lischka. Nonadiabatic Excited-State Dynamics with Hybrid ab Initio Quantum-Mechanical/Molecular-Mechanical Methods: Solvation of the Pentadieniminium Cation in Apolar Media. *J. Phys. Chem. A*, 114:6757, 2010.

[26] M. Barbatti, G. Granucci, M. Ruckenbauer, F. Plasser, R. Crespo-Otero, J. Pittner, M. Persico, and H. Lischka, 2008-2018. NEWTON-X - package for Newtonian dynamics close to the crossing seam, `http://newtonx.org`.

[27] T. E. Exner. Critical Investigation on the Pseudobond Approach for QM/MM and Fragment-Based QM Methods. *Int. J. Quant. Chem.*, 111(5):1002, 2011.

[28] O. Christiansen, H. Koch, and P. Jørgensen. The second-order approximate coupled cluster singles and doubles model CC2. *Chem. Phys. Lett.*, 243:409, 1995.

[29] A B Trofimov and J Schirmer. An efficient polarization propagator approach to valence electron excitation spectra. *J. Phys. B*, 28:2299, 1995.

[30] M. E. Casida. Time-dependent density functional response theory for molecules. In *Recent Advances in Density Functional Methods*, page 155. World Scientific, Singapore, 1995.

[31] M. Barbatti, G. Granucci, M. Persico, M. Ruckenbauer, M. Vazdar, M. Eckert-Maksić, and H. Lischka. The on-the-fly surface-hopping program system Newton-X: Application to ab initio simulation of the nonadiabatic photodynamics of benchmark systems. *J. Photochem. and Photobiol. A*, 190:228, 2007.

[32] TURBOMOLE V6.4 2012, a development of University of Karlsruhe and Forschungszentrum Karlsruhe GmbH, 1989-2012, `http://www.turbomole.com`.

[33] M. J. Frisch, G. W. Trucks, H. B. Schlegel, G. E. Scuseria, M. A. Robb, J. R. Cheeseman, G. Scalmani, V. Barone, B. Mennucci, G. A. Petersson, H. Nakatsuji, M. Caricato, X. Li, H. P. Hratchian, A. F. Izmaylov, J. Bloino, G. Zheng, J. L. Sonnenberg, M. Hada, M. Ehara, K. Toyota, R. Fukuda, J. Hasegawa, M. Ishida, T. Nakajima, Y. Honda, O. Kitao, H. Nakai, T. Vreven, J. A. Montgomery, Jr., J. E. Peralta, F. Ogliaro, M. Bearpark, J. J. Heyd, E. Brothers, K. N. Kudin, V. N. Staroverov, R. Kobayashi, J. Normand, K. Raghavachari, A. Rendell, J. C. Burant, S. S. Iyengar, J. Tomasi, M. Cossi, N. Rega, J. M. Millam, M. Klene, J. E. Knox, J. B. Cross, V. Bakken, C. Adamo, J. Jaramillo, R. Gomperts, R. E. Stratmann, O. Yazyev, A. J. Austin, R. Cammi, C. Pomelli, J. W.

Ochterski, R. L. Martin, K. Morokuma, V. G. Zakrzewski, G. A. Voth, P. Salvador, J. J. Dannenberg, S. Dapprich, A. D. Daniels, Ö. Farkas, J. B. Foresman, J. V. Ortiz, J. Cioslowski, and D. J. Fox. Gaussian 09 Revision E.01. Gaussian Inc. Wallingford CT 2009.

[34] M. Barbatti and H. Lischka. Nonadiabatic deactivation of 9H-adenine: A comprehensive picture based on mixed quantum-classical dynamics. *J. Am. Chem. Soc.*, 130:6831, 2008.

[35] E. Fabiano and W. Thiel. Nonradiative deexcitation dynamics of 9H-adenine: An OM2 surface hopping study. *J. Phys. Chem. A*, 112:6859, 2008.

[36] A. N. Alexandrova, J. C. Tully, and G. Granucci. Photochemistry of DNA fragments via semiclassical nonadiabatic dynamics. *J. Phys. Chem. B*, 114:12116, 2010.

[37] H. Satzger, D. Townsend, M. Z. Zgierski, S. Patchkovskii, S. Ullrich, and A. Stolow. Primary processes underlying the photostability of isolated DNA bases: Adenine. *Proc. Natl. Acad. Sci. U.S.A.*, 103:10196, 2006.

[38] M. Barbatti and S. Ullrich. Ionization potentials of adenine along the internal conversion pathways. *Phys. Chem. Chem. Phys.*, 13:15492, 2011.

[39] L. B. Clark, G. G. Peschel, and I. Tinoco. Vapor spectra and heats of vaporization of some purine and pyrimidine bases. *J. Phys. Chem.*, 69:3615, 1965.

[40] M. Barbatti, Z. Lan, R. Crespo-Otero, J. J. Szymczak, H. Lischka, and W. Thiel. Critical appraisal of excited state nonadiabatic dynamics simulations of 9H-adenine. *J. Chem. Phys.*, 137:22A503, 2012.

[41] J.-D. Chai and M. Head-Gordon. Systematic optimization of long-range corrected hybrid density functionals. *J. Chem. Phys.*, 128:084106, 2008.

[42] N. L. Evans and S. Ullrich. Wavelength dependence of electronic relaxation in isolated adenine using UV femtosecond time-resolved photoelectron spectroscopy. *J. Phys. Chem. A*, 114:11225, 2010.

[43] S. Mai, M. Richter, M. Ruckenbauer, M. Oppel, P. Marquetand, and L. González. SHARC: Surface Hopping Including Arbitrary Couplings - Program Package for Non-Adiabatic Dynamics,2014 ,`sharc-md.org`, 2014.

[44] G. Granucci, M. Persico, and A. Toniolo. Direct semiclassical simulation of photochemical processes with semiempirical wave functions. *J. Chem. Phys.*, 114:10608, 2001.

[45] H.-J. Werner, P. J. Knowles, G. Knizia, F. R. Manby, M. Schütz, P. Celani, W. Györffy, D. Kats, T. Korona, R. Lindh, A. Mitrushenkov, G. Rauhut, K. R. Shamasundar, T. B. Adler, R. D. Amos, A. Bernhardsson, A. Berning, D. L. Cooper, M. J. O. Deegan, A. J. Dobbyn, F. Eckert, E. Goll, C. Hampel, A. Hesselmann, G. Hetzer, T. Hrenar, G. Jansen, C. Köppl, Y. Liu, A. W. Lloyd, R. A. Mata, A. J. May, S. J. McNicholas, W. Meyer, M. E. Mura, A. Nicklass, D. P. O'Neill, P. Palmieri, D. Peng, K. Pflüger, R. Pitzer, M. Reiher, T. Shiozaki, H. Stoll, A. J. Stone, R. Tarroni, T. Thorsteinsson, and M. Wang. Molpro, version 2015.1, a package of ab initio programs, 2015. http://www.molpro.net.

[46] J. M. Wang, R .M. Wolf, J .W. Caldwell, P. A. Kollman, and D. A. Case. Development and testing of a general Amber force field. *J. Comput. Chem*, 25(9):1157, 2004.

[47] S. Pronk, S. Pall, R. Schulz, P. Larsson, P. Bjelkmar, R. Apostolov, M. R. Shirts, J. C. Smith, P. M. Kasson, D. van der Spoel, B. Hess, and E. Lindahl. GROMACS 4.5: a high-throughput and highly parallel open source molecular simulation toolkit. *Bioinformatics*, 29(7):845, 2013.

[48] G. Weber and F. J. Farris. Synthesis and spectral properties of a hydrophobic fluorescent probe: 6-propionyl-2-(dimethylamino)naphthalene. *Biochemistry*, 18:3075, 1979.

[49] P. Jurkiewicz, L. Cwiklik, P. Jungwirth, and M. Hof. Lipid hydration and mobility: An interplay between fluorescence solvent relaxation experiments and molecular dynamics simulations. *Biochimie*, 94:26, 2012.

[50] A. D. Becke. A new mixing of Hartree-Fock and local density-functional theories. *J. Chem. Phys.*, 98:1372, 1993.

[51] C. Adamo and V. Barone. Toward reliable density functional methods without adjustable parameters: The PBE0 model. *J. Chem. Phys.*, 110:6158, 1999.

[52] P. J. Stephens, F. J. Devlin, C. F. Chabalowski, and M. J. Frisch. Ab initio calculation of vibrational absorption and circular dichroism spectra using density functional force fields. *J. Phys. Chem.*, 98:11623, 1994.

[53] A. Schäfer, H. Horn, and R. Ahlrichs. Fully optimized contracted Gaussian basis sets for atoms Li to Kr. *J. Chem. Phys.*, 97:2571, 1992.

[54] K. Kowalski and P. Piecuch. New coupled-cluster methods with singles, doubles, and noniterative triples for high accuracy calculations of excited electronic states. *J. Chem. Phys.*, 120:1715, 2004.

[55] A. Klamt and G. Schüürmann. COSMO: A new approach to dielectric screening in solvents with explicit expressions for the screening energy and its gradient. *J. Chem. Soc., Perkin Trans. 2*, page 799, 1993.

[56] L. Bagatolli and E. Gratton. Two-photon fluorescence microscopy observation of shape changes at the phase transition in phospholipid giant unilamellar vesicles. *Biophy. J.*, 77:2090, 1999.

[57] K. Simons and M. J. Gerl. Revitalizing membrane rafts: New tools and insights. *Nat. Rev. Mol. Cell Biol.*, 11:688, 2010.

[58] T. Parasassi, G. De Stasio, G. Ravagnan, R. Rusch, and E. Gratton. Quantitation of lipid phases in phospholipid vesicles by the generalized polarization of Laurdan fluorescence. *Biophy. J.*, 60:179, 1991.

[59] J. P. M. Jämbeck and A. P. Lyubartsev. Derivation and systematic validation of a refined all-atom force field for phosphatidylcholine lipids. *J. Phys. Chem. B*, 116:3164, 2012.

[60] C. Vega and E. de Miguel. Surface tension of the most popular models of water by using the test-area simulation method. *J. Chem. Phys.*, 126:154707, 2007.

[61] G. Lamoureux, E. Harder, I. V. Vorobyov, B. Roux, and A. D. MacKerell. A polarizable model of water for molecular dynamics simulations of biomolecules. *Chem. Phys. Lett.*, 418:245, 2006.

[62] M. Barbatti, A. J. A. Aquino, and H. Lischka. The UV absorption of nucleobases: semi-classical ab initio spectra simulations. *Phys. Chem. Chem. Phys.*, 12:4959, 2010.

[63] L. Cwiklik, A. J. A. Aquino, M. Vazdar, P. Jurkiewicz, M. Pittner, J.and Hof, and H. Lischka. Absorption and fluorescence of Prodan in phospholipid bilayers: A combined quantum mechanics and classical molecular dynamics study. *J. Phys. Chem. A*, 115:11428, 2011.

Papers

Paper I

Felix Plasser, Rachel Crespo-Otero, Marek Pederzoli, Jiří Pittner, Hans Lischka and Mario Barbatti. Surface Hopping Dynamics with Correlated Single-Reference Methods: 9H-Adenine as a Case Study *Journal of Chemical Theory and Computation*, 10:1395, February 2014.

Paper II

Marek Pederzoli and Jiří Pittner. A new approach to molecular dynamics with non-adiabatic and spin-orbit effects with applications to QM/MM simulations of thiophene and selenophene *The Journal of Chemical Physics* 146:114101, March 2017.

Paper III

Marek Pederzoli, Lukáš Sobek, Jiří Brabec, Karol Kowalski, Lukasz Cwiklik and Jiří Pittner. Fluorescence of PRODAN in water: A computational QM/MM MD study *Chemical Physics Letters*, 597:57, February 2014.

Paper IV

Mirza Wasif Baig, Marek Pederzoli, Piotr Jurkiewicz, Lukasz Cwiklik, and Jiří Pittner. Orientation of Laurdan in Phospholipid Bilayers Influences Its Fluorescence: Quantum Mechanics and Classical Molecular Dynamics Study *Molecules* 23:1707, July 2018